Condensate droplet size distribution and heat transfer on hierarchical slippery lubricant infused porous surfaces

Condensate Droplet Size Distribution and Heat Transfer on Hierarchical Slippery Lubricant Infused Porous Surfaces

Yota Maeda[1], Fengyong Lv[2,3], Peng Zhang[2], Yasuyuki Takata[1,4], Daniel Orejon[4,5] *

[1]Department of Mechanical Engineering, Thermofluid Physics Laboratory, Kyushu University, 744 Motooka, Nishi-ku, Fukuoka 819-0395, Japan

[2]Institute of Refrigeration and Cryogenics, Shanghai Jiao Tong University, Shanghai 200240, China

[3]College of Urban Construction and Safety Engineering, Shanghai Institute of Technology, Shanghai 201418, China

[4]International Institute for Carbon-Neutral Energy Research (WPI-I^{2}CNER), Kyushu University, 744 Motooka, Nishi-ku, Fukuoka 819-0395, Japan

[5]Institute for Multiscale Thermofluids, School of Engineering, The University of Edinburgh, Edinburgh EH9 3FD, Scotland, UK

* Corresponding author: d.orejon@ed.ac.uk

Abstract

In recent years, slippery lubricant infused porous surfaces (SLIPSs) have received important attention due to their excellent performance in applications such as condensation, low friction, self-cleaning and anti-icing, which is owed to the presence of an infused lubricant or oil effectively decreasing the liquid-solid interactions and enhancing droplet mobility when compared to hydrophobic and/or to superhydrophobic surfaces. In this work, we fabricate and make use of hierarchical micro-/nano-structured and nano-structured SLIPSs for condensation phase-change. Optical microscopy and macroscopic experimental observations are coupled to extract the droplet size distribution at different condensation times. Heat transfer resistance

model through individual condensing droplets is further extended here to account for the presence of both micro- and nano-structures. Then, heat transfer through individual droplets is coupled to the droplet number density to estimate the heat transfer at different condensation times and their overall performance. A 100% greater heat transfer performance is reported on nano-structured SLIPSs when compared to hierarchical micro-/nano-structure SLIPSs due to the greater thermal resistance imposed by the micro-structures and the lubricant present within the structures. We conclude that although the presence of micro-structures shifts the droplet number density towards greater population of smaller sized droplets, this effect is not enough to overcome the greater heat transfer predicted on solely nano-structured SLIPSs. Findings presented here complement current research on SLIPSs and condensation phase-change and are of great importance for the effective design of SLIPSs with enhanced condensation heat transfer performance.

Keywords: Slippery Lubricant Infused Porous Surfaces, Condensation Phase-Change, Heat Transfer, Hierarchical SLIPS, Droplet Size Distribution, Heat Transfer Resistance Based Model

Nomenclature

Variables

S_{RMS}	average surface roughness [µm]
S_z	distance between the highest top and the lowest valley [µm]
f	solid fraction [-]
f_n	solid fraction of nano-structures [-]
φ_m	solid fraction of micro-structures [-]
θ_a	advancing contact angle [°]
θ_i	intrinsic contact angle on the flat hydrophobic surface [°]
θ_r	receding contact angle [°]
θ_e	average contact angle [°]
θ_{a_SHS}	advancing angle on SHS [°]
r	droplet radius [m]
r_e	effective droplet radius [m]
r_{range}	average droplet radius between the two extremes of the size range [m]
r_{min}	minimum radius for nucleation [m]
r_{max}	maximum experimental radius [mm]
T_{amb}	ambient temperature [K or °C]
T_{sub}	substrate temperature [K or °C]
T_{sat}	saturation temperature [K or °C]
ΔT	subcooling condition [K]
ΔT_c	difference of temperature due to the Kelvin effect [K]
RH	relative humidity [%]
N_s	nucleation density before coalescence [#/mm^2]
$n(r)$	droplet number density for sizes below the effective radius r_e [#/mm^3]
$N(r)$	droplet number density for sizes above the effective radius r_e [#/mm^3]
$N_{re}(r)$	number of droplets of certain radius r [#]
A	area of observation [mm]
t	time [min]
γ_{wa}	surface tension water-air [N/m]
ρ_w	density of the condensate [kg/m^3]
h_{fg}	latent heat of condensation [kJ/kg]
q''	theoretical surface heat flux [W/m^2]
q_d	heat transfer individual droplets [W]
$q_{d/n/c/l}$	heat transfer on nano-structured SLIPS [W]
$q_{d/m/n/c/l}$	heat transfer on micro-/nano-structured SLIPS [W]
R_i	interfacial thermal resistance for condensation [K/W]
R_d	droplet thermal resistance [K/W]
R_l	lubricant thermal resistance [K/W]
R_{Cu}	micro-structure thermal resistance [K/W]
$R_{m/n/c/l}$	micro-/nano-structures, hydrophobic coating and lubricant resistance [K/W]
$R_{n/c/l}$	nano-structures, hydrophobic coating and lubricant thermal resistance [K/W]
h_i	condensation interfacial heat transfer coefficient [W/m^2/K]
α	accommodation coefficient [-]
R_g	specific gas constant [J/kg/K]
ρ_v	water vapour specific density [kg/m^3]
k_w	water thermal resistance [W/m/K]
δ_l	thickness of the lubricant [m]
k_l	thermal conductivity of the lubricant [W/m/K]
δ_c	thickness of the hydrophobic coating [m]
k_c	thermal conductivity of the hydrophobic coating [W/m/K]
h_{CuO}	height of the nano-structures [m]
k_{CuO}	thermal conductivity of the copper oxide [W/m/K]
h_{Cu}	height of micro-structures [m]
k_{Cu}	thermal conductivity of copper [W/m/K]
a	droplet number density coefficient [-]
b	droplet number density slope [-]

Abbreviations

SLIPS	Slippery Lubricant Infused Porous Surface
SHS	Superhydrophobic Surface
FWC	Filmwise Condensation
DWC	Dropwise Condensation
VOCs	Volatile Organic Compounds
CAH	Contact Angle Hysteresis [°]
SI	Supplementary Information
GPL	General Purposes Lubricant
1D	One Dimensional

Introduction

Industrial and everyday applications such as power generation, air conditioning and electronics cooling rely on filmwise condensation (FWC) as the main condensation mechanism. FWC ensues on high surface energy materials such as copper, aluminium, titanium or stainless steel typically employed on the condenser side [1, 2]. Nonetheless, in the past decades, aiming to improve the heat transfer performance of the condenser, researchers have made use of hydrophobic coatings that can lower the energy of the surface prompting the continuous nucleation, growth and departure of the condensate via gravitational forces in a dropwise condensation (DWC) fashion[3-6]. Owing to the continuous condensate removal of millimetre droplets, DWC on hydrophobic surfaces provides greater heat transfer coefficients than FWC [7-9]. In addition to hydrophobic surfaces, micro-/nano-textured surfaces coated with a thin conformal hydrophobic layer, so called superhydrophobic surfaces (SHSs), have demonstrated to provide excellent low adhesion and enhanced condensation heat transfer performance when compared to both hydrophilic and hydrophobic surfaces [10-12]. While on hydrophobic surfaces droplets must grow to sizes in the order of a millimetre before the condensate sheds the surface, the extreme low adhesion of the condensate to SHSs can ensue removal of droplets via gravity and coalescence-induced droplet-jumping of droplets with sizes in the submillimetre/micrometre range [11, 13, 14] or even in the submicron range [15]. SHSs can enhance the overall condensation heat transfer performance up to 25% when compared to DWC on hydrophobic surfaces and up to 5 times when compared to FWC [11, 16, 17]. We note here that most heat transfer via condensation takes place for droplet sizes in the submillimetre range [2, 18, 19].

The excellent condensation heat transfer, water repellency, anti-fogging and anti-icing properties of SHSs are owed to the presence of air pockets entrapped within the hydrophobic micro- and/or nano-structures, which effectively decrease the solid-liquid binary interactions

and hence the adhesion of the condensate to the surface [20, 21]. In addition to SHSs, hydrophilic micropillared surfaces [22], hydrophobic-hydrophilic patterned wettability surfaces [23, 24], surfaces with ambiphilic micro-structures (hydrophilic micropillars with hydrophobic tops) [25, 26], nano-structured porous surfaces coated with a hydrophobic promoter layer [27], and/or superhydrophobic/superhydrophilic patterned wettability surfaces [14, 28, 29], are other approaches adopted for the control of the condensate aiming to improve the heat transfer performance during phase-change. More recently, continuous nucleation, growth and departure of droplets via gravity and/or coalescence-induced droplet-jumping in a DWC fashion was achieved on bare structured micro- and nano-structured copper oxide surfaces exposed to the ambient [30, 31]. Upon exposure to laboratory conditions, the adsorption of hydrophobic volatile organic compounds (VOCs) onto the copper oxide nano-structures mask the intrinsic hydrophilic wettability of the metal empowering the superhydrophobic properties of such engineered surfaces [30, 31]. The transition from hydrophilic to hydrophobic upon adsorption of VOCs was earlier reported on smooth metals and rare earth oxides by Preston *et al.* [32] while the transition from hydrophilic to superhydrophobic on boron nitride nanotubes was reported by Boinovich *et al.* [33].

If we now impregnate the micro- and/or the nano-structures of a SHS with a lubricant or an oil, a new range of low adhesion water-repellent surfaces coined slippery lubricant infused porous surfaces (SLIPSs) emerge [34, 35]. SLIPSs have been reported to provide extremely low adhesion between the liquid and the infused surface, prompting droplet self-removal for surface inclination angles as low as 5°, and offering very low contact angle hysteresis *ca*. 2.5° [36-38]. SLIPSs offer virtually no-pinning due to the smoothness of the lubricant layer and to the more affinity of the lubricant for the surface, *i.e.*, for the hydrophobic coating, hindering the condensate substrate intimate interactions [37, 39, 40]. Furthermore, SLIPSs surfaces can overcome the high adhesion of droplets sitting in the Wenzel state as per the recently reported

slippery Wenzel state on lubricant infused hierarchical micro- and nano-textured SLIPSs[13]. Some of the applications where SLIPSs excel are self-cleaning [41], drag reduction [42], anti-icing [43], water harvesting [44], along with their self-healing capabilities [35]. In addition to the abovementioned applications, SLIPSs are excellent candidates for condensation heat transfer providing up to 100% greater heat transfer coefficients for water when compared to hydrophobic and/or to SHSs [45], and 400% and 450% enhancement when compared to FWC for water and toluene, respectively [46]. The excellent low adhesion of SLIPSs performing in a DWC manner has also been proven even for low surface tension fluids such as: octane, hexane and pentane [39]. Thereafter, Weisensee *et al.* provided a coupled experimental and analytical methodology for the estimation of the heat transfer performance on SLIPSs as a function of the coating thickness and the solid fraction, reporting ca. 12 times better heat transfer when compared to FWC [2]. More recently, continuous DWC of low surface tension ethanol with the consequent enhancement in heat transfer performance has been reported on functionalised copper oxide nanostructured surfaces infused with Krytox^{TM} 1525 lubricant [47]. To recap, SLIPSs present important advantages when compared to hydrophobic surfaces and to SHSs such as: occurrence of DWC for low-surface tension fluids with quick droplet shedding opposed to FWC taking place on hydrophobic surfaces or SHSs [39, 46, 47]; occurrence of slippery Wenzel state while on SHSs droplets remain pinned to the structures, i.e., rose petal state [48]; self-healing properties as the lubricant film can wick into lubricant depleted zones or within structural damaged areas [35]; presence of a protective lubricant layer against corrosion preventing the direct interaction between the environment and the structured surface underneath the oil[49], as well as anti-icing [43] and anti-fouling and/or anti-scale [50] enhanced capabilities, owed to the reduced adhesion and interactions, etc. More specifically, in the context of this manuscript, we make use of SLIPSs as per their enhanced droplet mobility

of small droplets, i.e., greater droplet removal frequency, and enhanced droplet shedding velocities when compared to hydrophobic surfaces and to SHSs [51].

Aiming to better understand the interactions between fluids and SLIPSs, lubricant viscosity [2, 37, 48, 52], presence or absence of nano-structures on a micropillared surface [51], and the spacing between micro-structures [37], are some of the parameters previously addressed in the literature. The viscosity of the lubricant affects droplet mobility with greater shedding velocities in the case of low surface tension lubricants either upon droplet deposition on an inclined surface [37, 52] or during dynamic condensation [2, 39]. Smith *et al.* investigated the effect of micro-structure spacing upon droplet deposition on micro-posts (in absence of a nano-scale roughness) reporting a decrease in the roll-off angle as the spacing was increased [37]. By increasing the surface roughness, i.e., decreasing the solid fraction, Dai *et al.*, observed an increase in the apparent contact angle of deposited water droplets, which can be directly associated with a decrease in the effective droplet-SLIPSs adhesion[43]. Anand *et al.*, compared the condensation behaviour on a micro-/nano-structured SHS to that of a micro-/nano-structured SLIPS [51]. They reported on the effective droplet mobility of droplets below the submillimetre range on SLIPSs; whereas on SHSs, droplets with sizes above 3 millimetres were necessary in order to overcome the adhesion to the surface [51]. On other hand, a 10 fold increase in the amount of condensate collected was reported for condensation on slippery asymmetric bumps by combining the macroscopic bumps of the dessert beetle with the asymmetric features of a cactus spine and with the slippery nature of the pitcher plant when compared to a flat SLIPSs [53]. From the above literature, it is clear that the surface structure induces different droplet-surface adhesion as exemplified by the different apparent and rolling angles reported when increasing the spacing between structures, i.e., when decreasing the solid fraction [37, 48]. In essence, in this work, two cases where the effective area fraction is decreased as a consequence of the presence of micro-structures and lubricant oil present within

100 them are compared to two other cases with absence of micro-structures. In addition, and despite
101 of the extensive amount of experimental research carried out in the past 9 years on the
102 fundamentals of droplets on SLIPSs and on applied heat transfer, the presence of micro-
103 structures as in the work of Anand et al. [51] and the absence of micro-structures underneath
104 the infused lubricant as in the work of Weisensee et al. [2] during condensation have not been
105 compared to date. Hence, in the present work, we make use of SLIPSs fabricated following
106 facile and easy scalable etching and oxidation procedure as in the work of Zhu *et al.*, and in
107 our earlier works [54-57].

108 In the present work, two different SHSs varying in the size and density of the micro-
109 structures, *i.e.*, big size and high density of micro-structures and small size and low density of
110 micro-structures, were prepared. In addition, two nano-structured SHSs with similar size and
111 density of the nano-structures were also fabricated. After fabrication, SHSs were infused with
112 a low energy lubricant to create our SLIPSs. Finally, the condensation performance on all four
113 SLIPSs was addressed inside an environmental chamber by means of optical microscopy and
114 macroscopic experimental observations. From optical microscopy and macroscopic
115 experimental observations, the droplet number density, $N(r)$ [#/mm^3] at different time intervals
116 on the different SLIPSs, was extracted. Then, to estimate the overall heat transfer performance,
117 the droplet number density is coupled with steady-state heat transfer conduction analysis
118 through individual droplets. The heat transfer model adopted here has been extended to account
119 for the presence of both micro- and nano-structures, contrasting to earlier models where only
120 the micro-structures [58] or the nano-structures on a SHS [9, 18] and on a SLIPS [2] were
121 considered. Results show the better overall theoretical heat transfer performance of up to 100%
122 increase on nano-structured surfaces when compared to hierarchical micro-/nano-structured
123 SLIPSs. The worse heat transfer performance in the presence of micro-structures is owed to
124 the additional heat transfer resistance imposed by the greater thickness of the micro-structures

and the impregnated lubricant present within the micro-structures. Although the presence of micro-structures seems to shift the droplet size distribution towards greater droplet size numbers and smaller sizes, differences on the theoretical heat transfer through single droplets overweight that of the droplet number density at any given time. Last, the periodicity of the theoretical heat transfer calculations based on the different droplet number densities reported at different condensation times as a consequence of the continuous nucleation, growth and shedding of droplets in a DWC is presented and discussed for the first time. We conclude here on the greater overall theoretical heat transfer on solely nano-structured surfaces independent of the condensation time. Nonetheless, we would like to note that the observed shift of the droplet number density towards smaller droplet sizes on hierarchical micro-/nano-structured SLIPS, presumably due to the lower adhesion to the surface, might in turn induce quicker droplet shedding and improved heat transfer performance not captured by the overall theoretical heat transfer resistance based model.

Experimental Procedure

Surface fabrication

Two hierarchical micro- and nano-structured SHSs varying in the size and the density of the micro-structures were fabricated as in the work of Zhu *et al.* and Zhang *et al*. [54, 55, 57]. Pristine copper plates of 10 x 10 mm^2 and 500 μm in thickness were ultrasonicated in acetone, then in ethanol and lastly in distilled water prior to drying by nitrogen gas to remove any contaminant. Then, surfaces were immersed in a solution of 10 wt. % of HCl-H_2O to remove the oxide layer. Thereafter, samples were further cleaned in an ultrasonic bath with distilled water followed by drying with nitrogen gas. To create the different size and density of the micro-structures, samples were subjected to a easily-scalable wet etching in 0.48 wt % H_2O_2-H_2O and 1.89 mol/L HCl-H_2O solution as in Ref. 59 [59]. Bigger size and greater density of the micro-structures were conferred by dipping the copper substrate for longer time and at higher temperature (1 hour at 60 °C versus 20 minutes at 17 °C) [55, 57]. Next, to provide the surfaces with the necessary nanoscale roughness for the effective infusion and stability of the lubricant, both etched substrates were further oxidized in an aqueous solution of 2.5 mol/L NaOH-H_2O and 0.1 mol/L ($(NH)_4S_2O_8$-H_2O) for 30 minutes at 70 °C [54, 55]. In addition, to allow for comparison between hierarchical micro-/nano-structured SLIPSs to solely nano-structured ones, smooth copper plates, i.e., non-etched samples, were further oxidized in the same aqueous solution of 2.5 mol/L NaOH-H_2O and 0.1 mol/L ($(NH)_4S_2O_8$-H_2O) for 30 minutes at 70 °C (as the micro-structured ones) and for 50 minutes at 15 °C. We henceforth refer to the hierarchical micro-/nano-structured SLIPSs as Mn_{SLIPS} for high density and big size of micro-structures and as mn_{SLIPS} for small size and low density of micro-structures. While solely nanostructured SLIPSs are referred as n_{SLIPS} for the small size blade-like of nanostructures (similar to those on Mn_{SLIPS} and mn_{SLIPS}) and N_{SLIPS} for the large size needle-like nanostructures. After surface oxidation, all samples were immersed in a solution of 1% POTS(1H,1H,2H,2H-Perfluorooctyltriethoxysilane)-ethanol for 12 hours at ambient

temperature, rendering the intrinsic wettability of the micro- and the nano-structures hydrophobic [60, 61]. We note here that the hydrophobicity of the nano-structures is a necessary condition on the here fabricated SLIPSs in order to induce the more wetting affinity of the lubricant to the surface when compared to water [57]. All chemicals used during the fabrication procedure were purchased from Sinopharm Chemical Reagent Co., Ltd. (China).

Characterisation of SLIPSs before impregnation

The micro- and the nano-structure topography of Mn_{SLIPS}, mn_{SLIPS}, n_{SLIPS} and N_{SLIPS} before lubricant impregnation was assessed via Laser Optical Microscopy in a LEXT OLS4000 3D Laser Measuring Microscope from Olympus (Japan), and via Scanning Electron Microscopy (SEM) in a 3D Versa Dual Beam Environmental Scanning Electron Microscope from FEI Company (Hillsboro, Oregon, USA), respectively. Figure 1 includes 3D Laser Optical Microscopy profiles giving account of the different size and density of the micro-structures, while Figure 2 shows the surface nano-structures decorating the different surfaces:

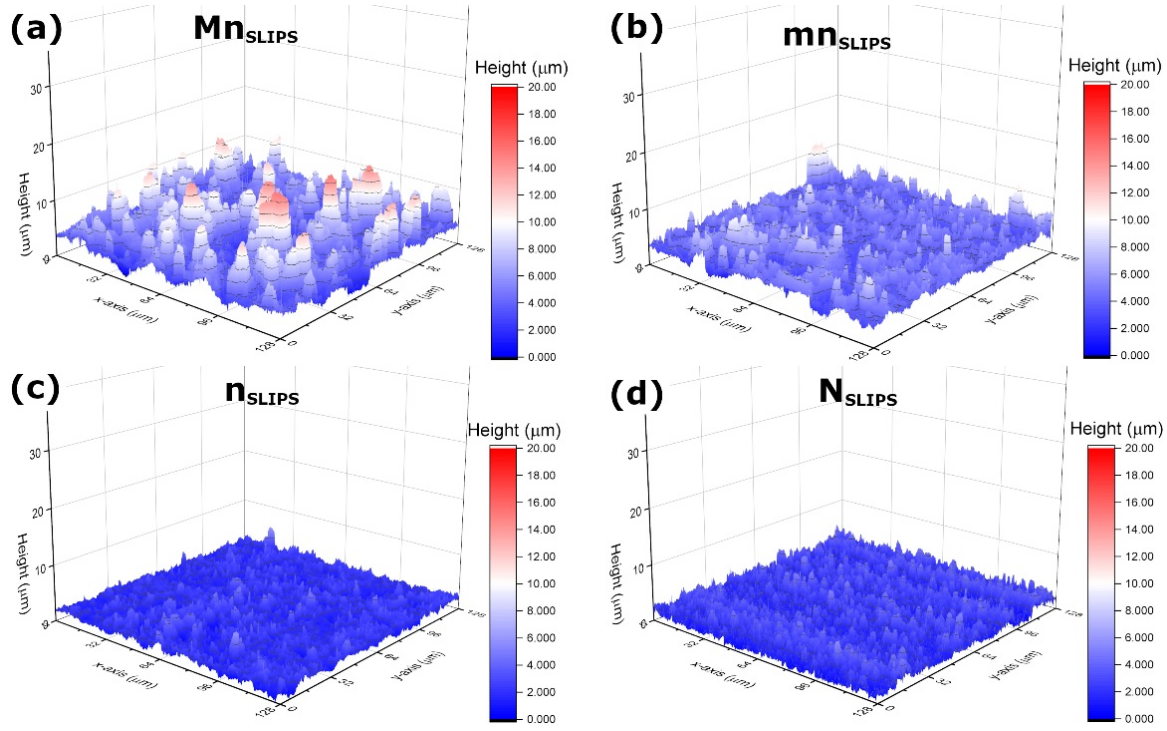

Figure 1 - 3D Laser Optical Microscopy on (a) Mn_{SLIPS}, (b) mn_{SLIPS}, (c) n_{SLIPS} and (d) N_{SLIPS}, prior to impregnation. Field of view is 128 x 128 µm² with a maximum height profile of 20 µm. Scale intensity of the height of the 3D surface profile changes from deep blue (0 µm) to red (20 µm).

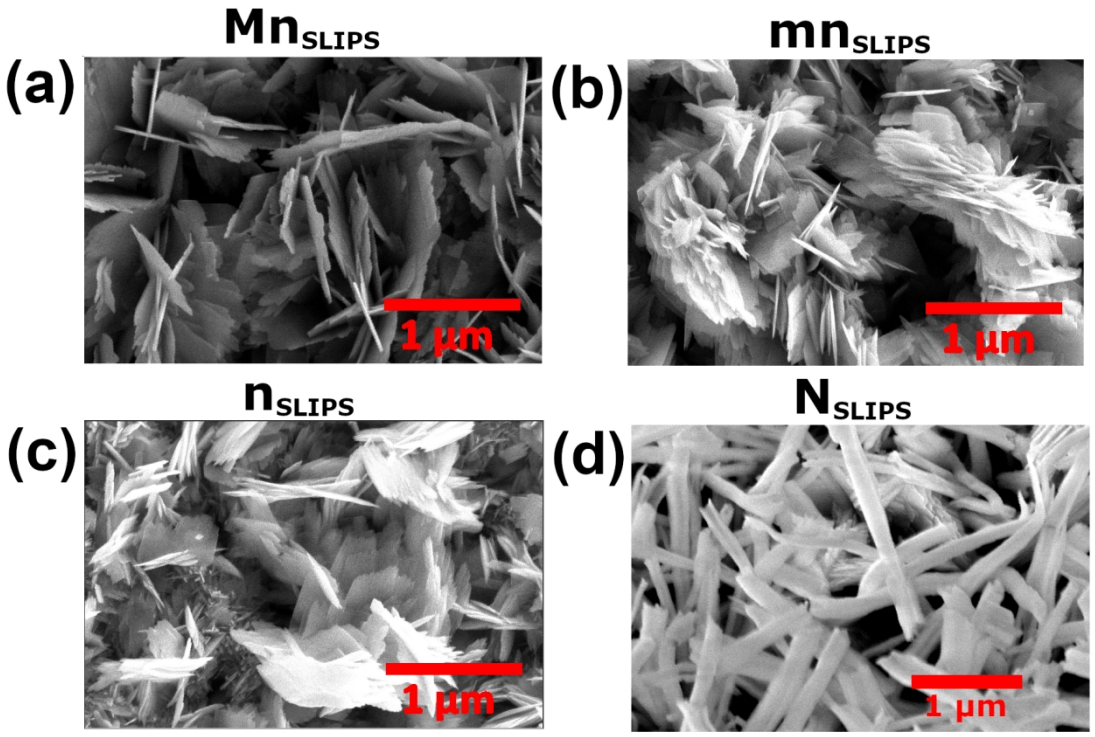

Figure 2 – High magnification Scanning Electron Microscopy (SEM) of the nanostructures decorating superhydrophobic (a) Mn_{SLIPS}, (b) mn_{SLIPS}, (c) n_{SLIPS} and (d) N_{SLIPS}, prior to impregnation. Scale bar is 1 µm.

From 3D Laser Optical Microscopy profiles presented in Figure 1, on one hand the greater size and density of the micro-structures on Mn_{SLIPS} (Figure 1a) when compared to mn_{SLIPS} (Figure 1b) a evident. Structures with height and lateral dimensions in the order of 20 micrometres are reported on Mn_{SLIPS}, while on mn_{SLIPS} height and lateral dimensions are kept below 10 micrometres as a consequence of the lesser time and lower temperature of the etching process. On the other hand, the absence of flower like micro-structures on n_{SLIPS} (Figure 1c) and on N_{SLIPS} (Figure 1d) when compared to Mn_{SLIPS} (Figure 1a) and mn_{SLIPS} (Figure 1b) is highlighted. Further surface characterisation including 2D Laser Optical Microscopy profiles of the four SLIPSs studied can be found in and Figure SI1 and Section SI.1 in the accompanying Supplementary Information (SI).When looking into the surface nano-structures included in Figure 2, of importance is to stress the similar geometry, size and density of the nano-structures decorating Mn_{SLIPS} (Figure 2a), mn_{SLIPS} (Figure 2b) and n_{SLIPS} (Figure 2c), which is owed to

198 the very same oxidation procedure followed. When comparing Mn_{SLIPS} (Figure 2a), mn_{SLIPS}
199 (Figure 2b) and n_{SLIPS} (Figure 2c) to N_{SLIPS} (Figure 2d) though, clear differences on the
200 geometry (blade-like versus needle-like nano-structures) while slight differences on the
201 random arrangement are revealed.

202 To provide further characterisation on the different surface structure depending on the
203 fabrication procedure, the average surface roughness S_{RMS} and the distance between the highest
204 top and the lowest valley S_z were extracted from 3D Laser Optical Microscopy, which are
205 included in Table 1. In addition, the solid fraction *f* before impregnation was estimated making
206 use of the Cassie-Baxter equation as $f = (\cos\theta_{a\_SHS} + 1)/(\cos\theta_i + 1)$[55, 62], where θ_{a_SHS}
207 is the advancing contact angle of the superhydrophobic surface without impregnation and θ_i is
208 the intrinsic contact angle on the flat hydrophobic surface equals 115° ± 3° [55]. The solid
209 fraction *f* for each of the structured surfaces fabricated before impregnation is then included in
210 Table 1. We note here that all surfaces before impregnation showed superhydrophobicity with
211 advancing contact angles above 155° as earlier reported [55].

212 **Characterisation of SLIPSs**

213 After etching, oxidation and hydrophobization of the surfaces, coated samples were immersed
214 in Krytox® General Purpose Lubricant 103 (GPL103) from DuPont™ (USA). GPL103 has a
215 density of 1.92 kg/dm^3 at 0 °C and a viscosity of 82 cSt at 20 °C. Next, advancing contact
216 angle, θ_a (°), and receding contact angle, θ_r (°), of the fabricated SLIPSs after impregnation
217 were measured in a custom-built goniometer and analysed using ImageJ snake-based approach
218 plugging[63, 64]. θ_a and θ_r were extracted from the shape of 3 microliter droplet sliding over
219 the different SLIPSs, which are included in Table 1. Standard deviations on θ_a, and θ_r were
220 obtained from 3 independent experiments.

221

Table 1 – Substrate characterization of Mn_{SLIPS}, mn_{SLIPS}, n_{SLIPS} and N_{SLIPS} as: S_{RMS} surface roughness (µm), S_z maximum distance between highest top and lowest valley of the micro-structures (µm), f solid fraction prior to oil impregnation. θ_a advancing contact angle (°) and θ_r receding contact angle (°) on slippery lubricant infused porous surfaces after impregnation.

	Mn_{SLIPS}	mn_{SLIPS}	n_{SLIPS}	N_{SLIPS}
S_{RMS} (µm)	2.1 ± 0.5	1.4 ± 0.3	0.8 ± 0.1	0.6 ± 0.1
S_z (µm)	16.8	10.7	-	-
f	0.13	0.12	0.11	0.10
θ_a (°)	114° ± 2°	117° ± 1°	118° ± 2°	118° ± 1°
θ_r (°)	111° ± 1°	114° ± 1°	115° ± 2°	115° ± 1°

From the wettability characterisation presented above we stress here that the presence or absence of micro-structures underneath the infused lubricant does not influence considerably the macroscopic θ_a and θ_r and/or the contact angle hysteresis (CAH) defined as CAH = θ_r - θ_a.

After characterising the surface structure and wettability of our SLIPSs, in order to fully describe the interactions between sessile droplet and our SLIPSs, we further discuss on the interactions between water droplets, the lubricant and the surface. On one hand, to satisfy the stability of the SLIPSs upon interaction with water, the immiscibility between the lubricant and water must be ensured, hence we make use of Krytox® GPL103 as per its earlier reported immiscibility in water [65]. On the other hand, a layer of lubricant may develop over the droplet, which is known as cloaking [37, 40, 65]. For moderate and high surface energy lubricant, the spreading coefficient is typically negative and hence the encapsulation of the droplet by the lubricant does not occur [37]. Whereas for a low surface tension lubricant and hence a positive spreading coefficient, the lubricant does typically cloak/encapsulate the droplet [37]. In the present cases, cloaking of the droplet by a thin lubricant film is expected [48, 57, 65]. The thin nature of the cloaking film in the order of tens of nanometres should in turn not influence considerably the theoretical heat transfer performance proposed here [2, 40].

Experimental apparatus and procedure

All experimental observations were carried out in an environmental chamber PR-3KT from ESPEC Corp. (Japan). Inside the environmental chamber, a custom-built Peltier stage, connected to a PID controller and to a cooling bath both located outside the chamber, is placed vertically. A custom-built copper block of the same area as the SLIPS samples (10 x 10 mm^2) was inserted in a thermally insulating TEFLON block both with thicknesses of 10 mm and attached to the Peltier stage to ensure 1 dimensional (1D) heat transfer between the Peltier stage and the SLIPSs. A thermocouple was then set at the centre of the copper block few millimetres below the SLIPS sample. Then, SLIPSs was attached to the copper block using double side carbon tape. To ensure homogenous conditions within the chamber, prior to condensation experimental observations, the temperature T_{amb} and the relative humidity RH of the ambient air inside the chamber, i.e., in the presence of non-condensable gases, were set at 30 °C ± 1 °C and at 90% ± 5% respectively for 30 minutes. While the substrate temperature T_{sub} was set at 35 °C, which is above the water dew temperature so to avoid any condensation. Thereafter, T_{sub} was lowered to 5 °C, environmental chamber was turned off and experimental observations were recorded. We note here that in spite of the environmental chamber being turned off to avoid any vibration, the overall relative humidity was within ± 5% for the entire duration of the experiments. However, locally near the surface, the concentration of the water vapour may be lower than that reported by the chamber. In addition, the use of a non-long working distance lens for the optical microscopy observations may also shield the homogeneous diffusion of water vapour towards the surface.

To allow for the acquisition of the experimental observations, a CCD camera Sentech STC-MC152USB with a resolution of 1360 x 1024 pixels was utilised. On one hand, optical microscopy experimental observations were acquired by making use of a Keyence high-resolution optical microscopy zoom lens VH-Z500R with a field of view of (590 ± 5) x (445 ±

5) μm^2 while a halogen lamp was used for coaxial illumination. On the other hand, a RICOH lens with a 30 mm spacing and a LED light were used for experimental observations at the macroscale with a field of view of (5.0 ± 0.1) x (3.8 ± 0.1) mm^2. A snapshot of the experimental setup inside of the chamber comprising: Peltier stage, optical microscope lens, CCD camera, x-y stage, tubing, cables and connections is found in Figure 3a; while detailed schematics of the complete setup is presented in Figure 3b. Snapshot including experimental setup and schematics for macroscopic experimental observations can be found in Figure SI2 in Section SI.2 in the accompanying SI.

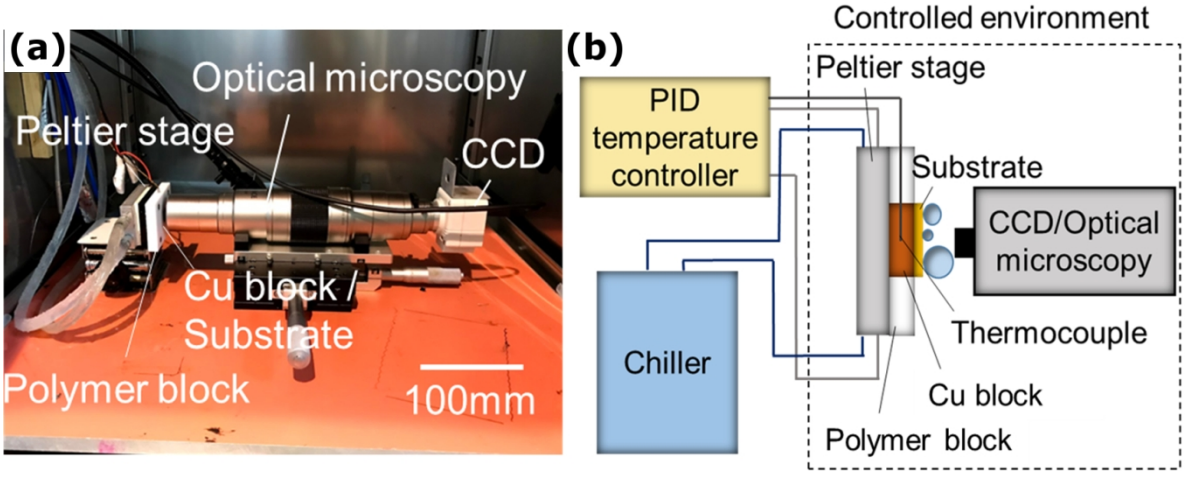

Figure 3 – (a) Snapshot of the experimental setup inside the environmental chamber including Peltier stage, electrical connections, thermocouple connected to PID controller, water pipes connected to chiller, Copper-TEFLON block, SLIPS sample, CCD camera and optical microscope zoom lens VH-Z500R for microscopic observations. (b) Schematic of the complete experimental setup including environmental chamber, PID controller and chiller. Scale bar in Figure 3a is 100 mm. Snapshot and schematics of the experimental setup for macroscopic experimental observations equipped with the RICOH lens and 30 mm spacing can be found in Figure SI2 in Section SI.2 in the SI.

Optical microscopy and macroscopic experimental observations were used to accurately determine the droplet size distribution, *i.e.*, droplet number density $N(r)$ [#/mm^3] for the estimation of the theoretical heat transfer performance [2, 18, 66]. The droplet number density $N(r)$ [#/mm^3] and the size of the droplets on our SLIPSs were extracted using Image-Pro

289 Plus[67] as follows. At different intervals of time, characteristic *instantaneous* snapshots were
290 analysed. From optical microscopy snapshots, the size and the number of droplets ranging
291 between 5 to 200 μm in radius were extracted by manually fitting circles to the contour of the
292 condensing droplets. In addition, to provide a more accurate characterisation of droplets with
293 sizes in the order of tens of micrometres and below, optical microscopy areas were analysed
294 applying a 4x magnification. On other hand, macroscopic observations were utilised to extract
295 the size and the number of droplets with radius ranging from 50 μm to 1 mm. Due to the
296 different droplet sizes and a single plane of view, the radius of the droplet is estimated with
297 ±10% accuracy. Data extracted using Image-Pro Plus was then imported to Origin and plotted.
298 More details on the procedure followed for the analysis of the droplet number density can be
299 found in Section SI.3 in the accompanying SI.

300

Results

Condensation Dynamic Observations and Droplet Number Density Characterisation

Characteristic optical microscopy snapshots during condensation on Mn_{SLIPS}, mn_{SLIPS}, n_{SLIPS}, and N_{SLIPS} at different condensation times t = 1, 10, 30 and 60 minutes, with t = 0 minutes as the onset of nucleation, are presented in Figure 4:

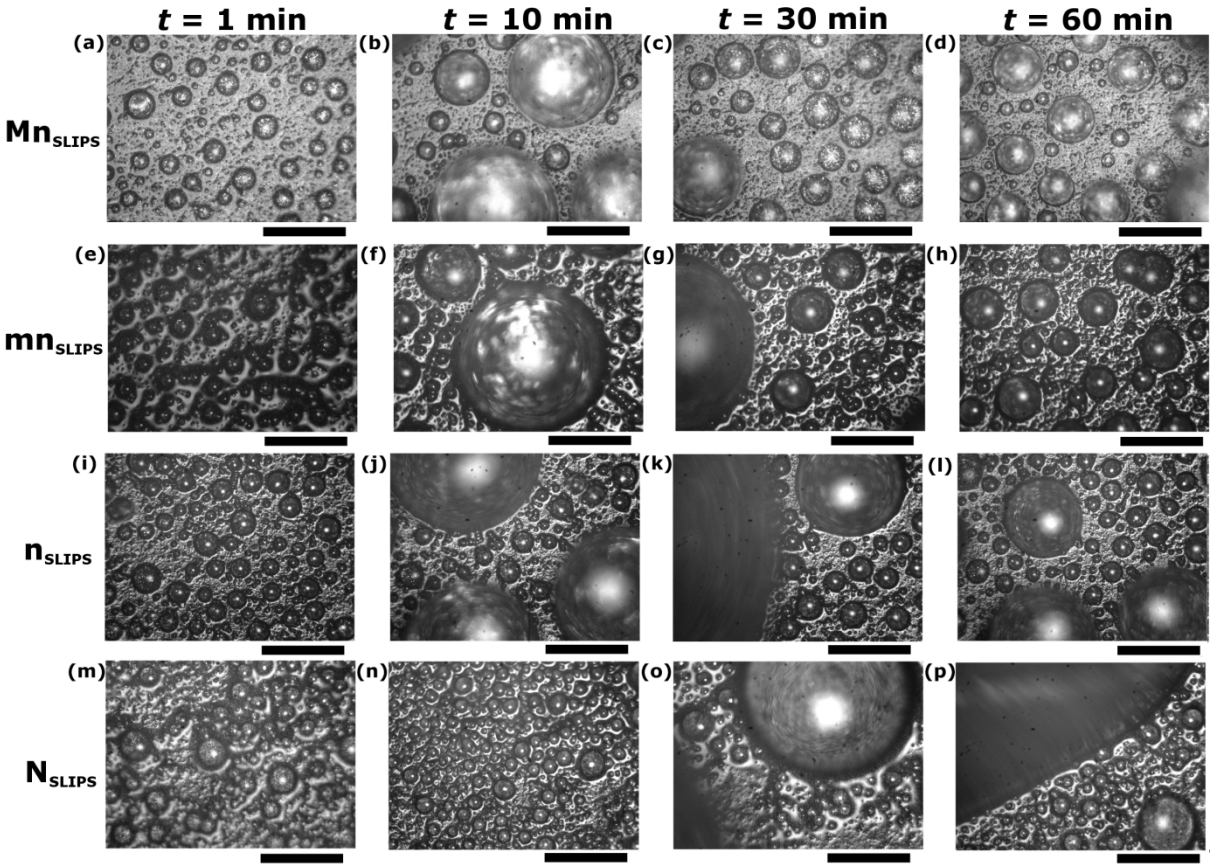

Figure 4 – Characteristic optical microscopy snapshots of water condensation on (a-d) Mn_{SLIPS}, (e-h) mn_{SLIPS}, (i-l) n_{SLIPS} and (m-p) N_{SLIPS} at 1 minute, 10 minutes, 30 minutes and 60 minutes with t = 0 seconds as the onset of nucleation. Scale bars are 200 µm.

When looking into optical microscopy experimental observations, a similar qualitative condensation behaviour on all SLIPSs is reported. Heterogeneous nucleation takes place evenly all over the surface on all four samples. The minimum radius for nucleation $r_{\min}$ can be estimated by making use of Kelvin's equation as: $r_{min} = {}^{2\gamma_{wa}T_{sat}}\!/_{\rho_w h_{fg}\Delta T}$, where γ_{wa} is the

surface tension water-air, T_{sat} is the saturation temperature of the vapour, ρ_w is the density of the condensate, h_{fg} is the latent heat of gas to liquid phase-change and ΔT is the subcooling condition imposed, i.e., difference of temperature between the vapour T_{sat} and the condenser substrate T_{sub} [68-70]. Hence, for the same substrate temperature and environmental conditions reported here, $r_{min} \approx 0.7$ nm independently of the SLIPS studied, which cannot be resolved from optical microscopy observations. Then, as condensation develops, droplets grow via direct condensation until they reach the effective transition radius, r_e, which is directly related to the nucleation density N_s before any coalescence takes place as: $r_e = 1/\sqrt{4N_s}$ [2, 16, 19, 71]. Thereafter, droplets grow via direct condensation and via coalescence with neighbouring ones (Figure 4a,e,i,o).After several minutes from the onset of condensation, droplets in the order of tens to hundreds of micrometres can be observed as in Figure 4b,f,j,o. As two or more droplets coalesce, due to the low adhesion of the condensing droplets to the SLIPSs, the droplet contact line is able to depin and retract. Then new area in the vicinity of the recent coalesced droplet is available for re-nucleation and growth of small droplets. Eventually big droplets disappear from the field of view as when comparing Figure 4b&c, Figure 4g&h and Figure 4 k-l. From optical microscopy (area field of view 590 x 445 μm^2) we cannot precisely state if droplets are actually being removed by gravity, by sweeping or by coalescence with other neighbouring droplets. Further observations making use of macroscopic experiments were coupled with those at the micro-scale. An average shedding frequency of 4 ± 1 for Mn_{SLIPS}, 5 ± 1 for mn_{SLIPS}, 3 ± 1 for n_{SLIPS} and 3 ± 1 for N_{SLIPS} droplets per hour (major shedding events averaged from 4 hours of experimental observations), demonstrated the cyclic nucleation, growth, coalescence and shedding of the condensate occurring within the first 30 minutes. Hence droplet number density analysis is here carried out and presented for the first 30 minutes.

To evaluate the condensation performance on each of the structured surfaces studied, we extract the droplet number density function of the droplet radius $N(r)$ [#/mm^3] from optical

microscopy and from macroscopic experimental observations as $N(r) = {N_{\mathrm{re}}(r)/A}\,/\,{r_{\mathrm{range}}}$. Where $N_{\mathrm{re}}(r)$ is the droplet density or number of droplets of certain radius r, A is the area of observation equals to the optical microscopy or to the macroscopic field of view adopted during the experimental observations and r_{range} is the average droplet radius between the two extremes of the size range at which the droplet number density $N_{\mathrm{re}}(r)$ was retrieved. $N(r)$ [#/mm^3] relates then to the number and to the size of the droplets. The droplet number density $N(r)$ [#/mm^3] is eventually used to estimate the theoretical heat transfer performance [2, 9, 18, 19].

Next, the droplet number density $N(r)$ [#/mm^3] versus droplet radius r [µm] is plotted in Figure 5 for $\mathrm{Mn_{SLIPS}}$, $\mathrm{mn_{SLIPS}}$, $\mathrm{n_{SLIPS}}$, and $\mathrm{N_{SLIPS}}$ at t = 1, 5, 10, 15, 22 and 30 minutes along with their average over the presented times:

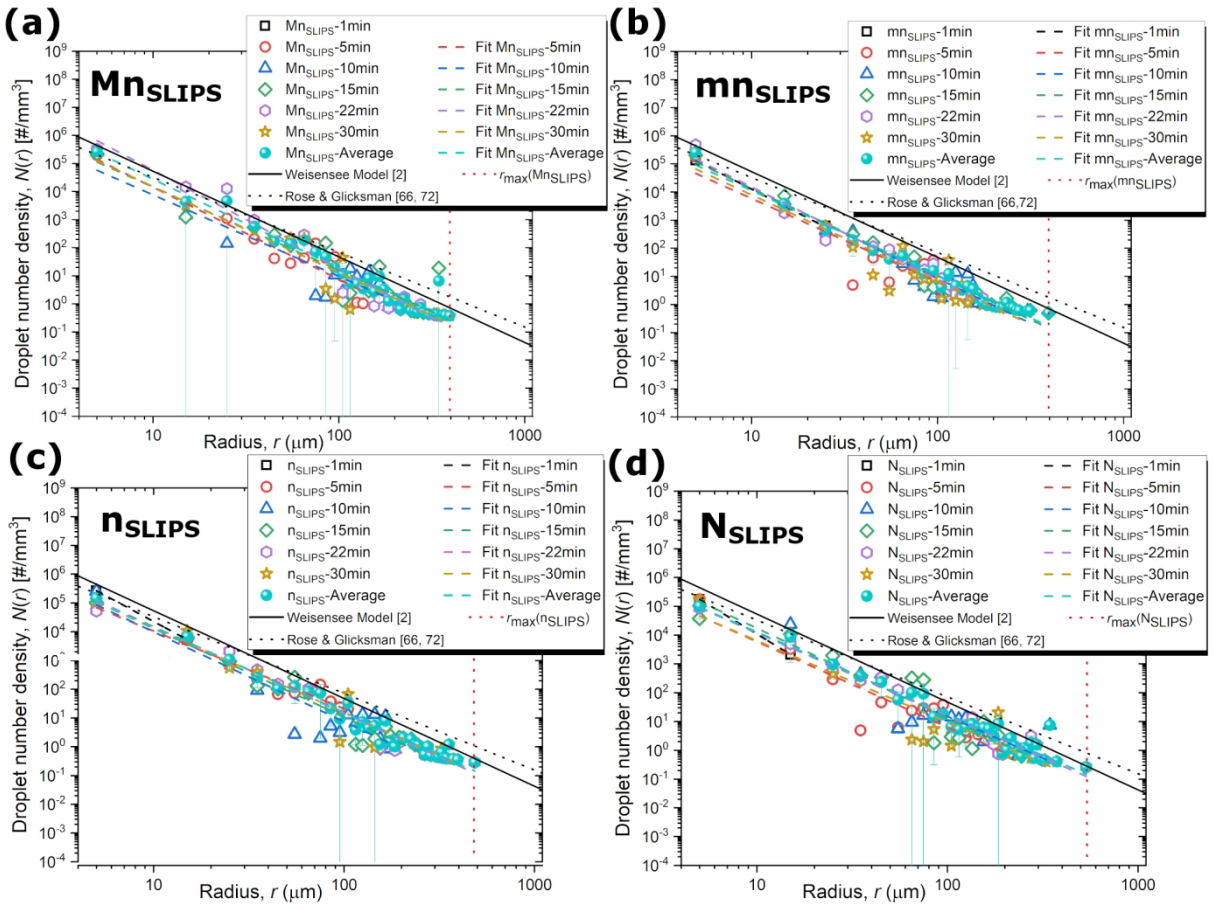

Figure 5 – Droplet number density, $N(r)$ [#/mm^3], versus droplet radius, r [µm], extracted by Image-Pro Plus[67] for (a) $\mathrm{Mn_{SLIPS}}$, (b) $\mathrm{mn_{SLIPS}}$, (c) $\mathrm{n_{SLIPS}}$, and (d) $\mathrm{N_{SLIPS}}$ at t = 1 (black squares),

5 (red circles), 10 (blue up-triangles) 15 (green rhomboids), 22 (purple hexagons), 30 (gold stars) minutes, and the averaged droplet number density (cyan spheres). Coloured dashed lines are included to illustrate the power law trends for the different condensation times and average one. In addition, droplet number density power-law fitting proposed by Weisensee *et al.* is included in black solid line [2] and correlation developed by Rose and Glicksman is included in black dotted line [66, 72]. In vertical red dotted lines, the maximum experimental radius, r_{max}, obtained from macroscopic observations of droplet shedding is represented. For a more direct comparison between the different droplet number densities on the different SLIPSs, the reader is referred to Figure 7b of the manuscript. Error bars represent the droplet number density standard deviation for the averaged case. Note error bars below x-axis as per the standard deviation in the same order of magnitude as the averaged values.

From Figure 5, the droplet number density follows a similar qualitative behaviour regardless of the surface micro- and/or nano-structure underneath the lubricant and the condensing droplets. Reported trends on Mn_{SLIPS}, mn_{SLIPS}, n_{SLIPS}, and N_{SLIPS} are in qualitative agreement with the model proposed by Rose and Glicksman where $N(r) = {}^{1}\!/_{3\pi r_e^2 \hat{r}}\left({}^{r}\!/_{\hat{r}}\right)^{-2/3}$ [66, 72], and the power-law fitting and average droplet density function included in the work of Weisensee *et al.*[2] (see Figure 5 and Figure 7b). Where $\hat{r} = r_{max}/1.3$ and r_{max} is calculated as: $r_{max} = \left({}^{6(\cos\theta_r - \cos\theta_a)\sin\theta_e \gamma_{wa}}\!/_{\pi(2 - 3\cos\theta_e + \cos\theta_e)\rho_l g}\right)^{0.5}$ with θ_e as the average contact angle between the advancing and receding contact angles estimated as: $\theta_e = \cos^{-1}(0.5\cos\theta_a + 0.5\cos\theta_r)$.

We highlight here that neither the different micro-/nano-structures underneath the condensing droplets nor the different experimental conditions influenced qualitatively the intrinsic droplet number density, although some quantitative differences may arise from the different subcooling and environmental conditions[8, 66]. All trends follow: $N(r) = ar^{-b}$, where b represents the inclination of the slope and dictates how the droplet number density changes with droplet size, while a is a coefficient in the order of 10^7 [2]. From Figure 5 it can

379 also be extracted that at early stages of condensation, *i.e.*, t = 1 minute, experimental coefficient
380 b is greater than for developed condensation times with values ranging between 3.2 and 4.0.
381 This is due to the great number of small droplets with sizes in the order of tens of micrometres
382 experiencing their initial growth and to the absence of droplets with sizes above tens of
383 micrometres. For greater condensation times, *i.e.*, $t \geq 5$ minutes, the average and standard
384 deviation of the coefficient b can be quantitatively compared to those earlier reported in
385 literature, which are further discussed below [2, 72-74]. Table 2 includes the different a and b
386 coefficients extracted from experimental observations for t = 5, 10, 15, 22 and 30 minutes for
387 Mn_{SLIPS}, mn_{SLIPS}, n_{SLIPS} and N_{SLIPS}:

388 **Table 2 – Fitting coefficients a and b extracted from experimental observations at t = 5, 10, 15,**
389 **22 and 30 minutes and averaged one, following the trend $N(r) = ar^{-b}$ for Mn_{SLIPS}, mn_{SLIPS},**
390 **n_{SLIPS} and N_{SLIPS}. Standard deviation for a and b coefficients are estimated as ± 1x10^7 and ± 0.16.**

	Mn_{SLIPS}		mn_{SLIPS}		n_{SLIPS}		N_{SLIPS}	
	a	b	a	b	a	b	a	b
t = 5	2.73x10^7	3.28	5.51 x10^6	2.97	5.27x10^6	2.7	5.51 x10^6	2.97
t = 10	6.17x10^6	2.90	2.01 x10^7	3.19	1.30x10^7	3.12	9.47 x10^6	2.90
t = 15	1.33x10^7	2.96	1.75 x10^7	3.11	1.54x10^7	3.08	2.22 x10^7	3.10
t = 22	1.51x10^8	3.45	2.91 x10^7	3.28	1.58x10^7	3.02	9.41 x10^6	2.89
t = 30	1.73x10^7	3.06	9.35 x10^6	3.07	1.27x10^7	2.96	4.45 x10^6	2.84
Average	3.74x10^7	3.14	1.18 x10^7	3.02	1.53x10^7	2.97	9.26 x10^6	2.86

391

392 Coefficients b calculated for Mn_{SLIPS}, mn_{SLIPS}, n_{SLIPS} and N_{SLIPS} included in Table 2 are
393 within the standard deviation and in agreement with the work of Weisensee *et al.* where b
394 equals 3.05 [2]. The less inclined slope reported in the case of nano-structured n_{SLIPS} and N_{SLIPS}
395 is, on the other hand, attributed to the presence of greater number of big droplets over the
396 intervals of time studied. In the case of n_{SLIPS} and N_{SLIPS}, droplets seem to be less mobile due

to stronger pinning to the surface when compared to Mn_{SLIPS} and mn_{SLIPS}. The greater *b* coefficients reported here (Table 2) when compared to the works of Tanaka, Watanabe *et al*. and Tanasawa (reported values between 2.6 and 2.7) are attributed to the better mobility of the droplets in the submillimetre range on SLIPSs when compared to smooth hydrophobic surfaces with shedding sizes above a millimetre [73-75]. When looking into the *a* coefficient, average values reported in Table 2 are found within the same order of magnitude to those reported by Weisensee *et al*. equal 6 x 10^7, although the magnitude of the our coefficients is 2 to 5 times lower as a consequence of the lower subcooling, absence of artificial sweeping and/or the different heat flux conditions imposed [2, 76]. On one hand, when looking into the *instantaneous* droplet number densities reported at different condensation times (*t* = 5, 10, 15, 22 and 30 minutes), for droplets with sizes equal or smaller than 100 μm, quantitative differences are found when comparing the coefficient *a* reported in Table 2. More specifically, by making use of $N(r) = ar^{-b}$ and for a given radius of 1 μm, up to two orders of magnitude difference in the droplet number density is put forward. On the other hand, the rather uniform *instantaneous* droplet number densities reported in Figure 5 for droplets with sizes equal or above 100 μm, opposed to the large variability on the droplet number distribution after a shedding event, is attributed to the field of view adopted during the macroscopic experimental observations. The width of the observation area is approximately 5 mm while the size of the shedding droplets is ca. 1 mm. Hence, after a shedding event, only a fraction of the surface (between $1/5^{th}$ and $1/3^{rd}$) is actually refreshed while the droplet number density remains the unaltered on the non-refreshed area, which in turn returns the observed rather homogeneous distribution throughout the *instantaneous* snapshots. Variations in the droplet number density at different condensation times were earlier pointed out by Rose and by other authors who proposed the use of a *steady*/average droplet number density for the calculations of the theoretical heat transfer in order to account for the variability of the droplet number density as

422 a consequence of the shedding/sweeping cycles [2, 66, 74, 77]. For a more direct comparison
423 between the different droplet number densities function of the SLIPSs, the reader can refer to
424 Figure 7b of the present manuscript. We note that the low magnification used in the
425 experiments did not allow for the accurate measurement of droplets with sizes below few
426 micrometres and/or for the observation of the self-propulsion of micro-droplets during
427 dropwise condensation on SLIPSs recently reported [78].

428 For the condensation times reported here, no appreciable shift of the DWC performance was
429 observed as a consequence of structure damage, peeling of the coating and/or oil depletion,
430 which in turn would induce the further pinning of the condensate and eventual FWC. In
431 addition, long-term condensation test was performed overnight for 11 hours on n_{SLIPS} showed
432 continuous DWC performance at any given condensation time under optical microscopy. As a
433 consequence of the optical microscopy technique utilized here, the extent of pinning and
434 whether there is a shift on the maximum experimental radius r_{max} could not be resolved, which
435 could be the scope for future research on the durability and stability of SLIPSs. To this extent,
436 we would like to remind the reader here that we recently demonstrated the feasibility of
437 operation of up to 192 hours within 16 experimental runs without appreciable change on the
438 overall heat transfer resistance of a two-phase closed thermosiphon paired with a
439 superhydrophilic evaporator and a SLIPS condenser. SLIPS condenser was fabricated and
440 impregnated following the very same procedure as the SLIPSs reported in this work [57].

441

442 **Steady State Heat Transfer through Condensing Droplets**

443 Next, we estimate the theoretical surface heat flux at the different condensation times on
444 each of our SLIPSs. The theoretical surface heat flux, q'' (kw/m^2), can be calculated from
445 coupling the individual droplet heat transfer function of their radius, $q_d(r)$, to the droplet

number density $N(r)$ as: $q'' = \int q_d(r)N(r)dr$ [2, 71]. Since typically during dropwise condensation droplet growth takes place via direct condensation for small droplet with radius below the transition radius r_e ($r < r_e$) and via droplet coalescence for droplets with radius above r_e ($r > r_e$), the total heat flux for dropwise condensation without taking into account droplet shedding or sweeping is expressed as [19, 79]:

$$q'' = \int_{r_{min}}^{r_e} q_d(r)n(r)dr + \int_{r_e}^{r_{max}} q_d(r)N(r)dr \qquad \text{Eq. 1}$$

where $n(r)$ and $N(r)$ are the droplet number density or droplet size distribution of droplets below and above the transition radius r_e, respectively. The transition radius r_e is calculated from the nucleation site density N_s obtained before the first coalescence event taking place typically before the first minute of the experimental observation as: $r_e = 1/\sqrt{4N_s}$ equals 5.4 μm, 5.7 μm, 5.0 μm and 5.1 μm on Mn_{SLIPS}, mn_{SLIPS}, n_{SLIPS} and N_{SLIPS}, respectively. r_e values are in agreement with those reported in Ref. 2 between 0.5 and 10 μm [2]. Last, r_{max} and r_{min} are defined as the maximum and minimum radius for droplet shedding and for heterogeneous nucleation to occur, respectively [8, 68, 70, 80].

On one hand, the droplet size distribution above the transition radius $N(r)$ can be extracted from Figure 5 or from the different coefficients reported in Table 2, while the droplet size distribution for droplets below the transition radius $n(r)$ can be estimated from the expressions proposed by Graham and Griffith [8], Tanaka [73], Kim and Kim [19], Miljkovic *et al*. [81], Wen *et al.* [71], Chavan *et al.*[18], and Alizadeh-Birjandi [82], amongst others. Nonetheless, in order to solely rely on our experimental data avoiding the use of empirical correlations, in this work we only make use of the $N(r)$ reported in Figure 5 for droplets bigger than r_e.

On the other hand, the heat transfer through a single droplet q_d can be calculated adopting a heat transfer thermal resistance based model for a droplet condensing on a hydrophobic surface developed by Kim and Kim [2, 9, 19]. On nano-structured SHSs though, q_d can then be

469 determined by making use of Kim and Kim's model adapted to account for the presence of
470 nano-structures as in the work of Miljkovic and Wang [9, 83]; while Weisensee *et al.* developed
471 a more appropriate model for nano-structured lubricant infused surfaces [2]. Nonetheless, the
472 presence of both micro-structures and nano-structures was not accounted for on earlier models,
473 which is one of the contributions of the present work. For the development of the heat transfer
474 resistance based model, the following assumptions/simplifications apply:

475 • the heat transfer resistance across the lubricant with thickness in the order of tens of
476 nanometres cloaking the droplet [40, 57] can be neglected as we are comparing droplets
477 with similar geometric configurations and the size of the droplets is at least two orders of
478 magnitude greater than the thickness of the film;

479 • the heat transfer resistance across the lubricant confined between the top of the nano-
480 structures and the condensing droplets is also neglected as the ternary configuration
481 surface-lubricant-water studied here behaves in the impregnated emerged state, *i.e.*, the
482 lubricant impregnates the structures but does not encapsulate their tops [37];

483 • the presence of a layer of Cu_2O earlier reported in the work of Enright *et al*. is also
484 neglected as all four SLIPSs have been fabricated under similar conditions hence the
485 similar thickness of the Cu_2O layer and hence comparable heat transfer resistance [16];

486 • interfacial resistances between the droplet and the oil, the droplet and the solid surface,
487 and the oil and the solid surface can be neglected when compared to the other thermal
488 resistances, as assumed in the widely adopted thermal resistance based models [2, 9, 18,
489 19, 83].

490 After the above stated assumptions, schematics of the heat transfer resistance based model
491 in the absence and in the presence of micro-structures on our SLIPSs can be found on Figure
492 6a and Figure 6b, respectively. The complete schematics of the heat transfer resistance-based

model through a single droplet and simplified one along with the relevant assumptions can be found in Section SI.4 in the accompanying SI as Figure SI4 and Figure SI5, respectively.

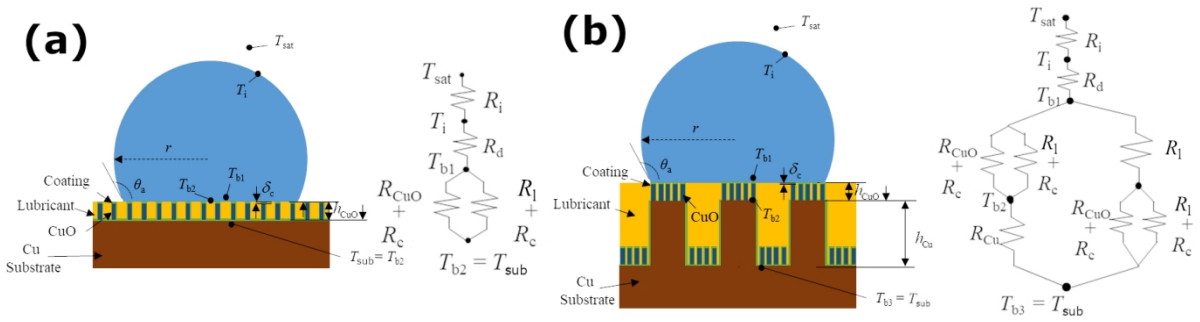

Figure 6 – Schematics of the heat transfer resistance based model adopted for the calculation of the thermal resistance thorough a single condensing droplet exerted by (a) the nano-structures, the hydrophobic coating, the lubricant and the droplet, and (b) the micro- and the nano-structures, the hydrophobic coating, the lubricant and the droplet.

From Figure 6 it is clear that the thermal resistance through the bulk copper and the condensing droplets is then function of the presence or absence of micro-structures. The heat transfer resistance through an individual droplet making use of the heat transfer resistance base model presented in Figure 6 can be then calculated as in Eq. 2:

$$q_{\mathrm{d}} = \frac{\Delta T}{R_{\mathrm{tot}}} = \frac{\Delta T}{R_{\mathrm{i}} + R_{\mathrm{d}} + R_{\mathrm{l}} + R_{\mathrm{m/n/c/l}}} \qquad \text{Eq. 2}$$

where R_{tot} is the total heat transfer resistance accounting for: R_{i} as the interfacial thermal resistance for condensation, R_{d} as the thermal resistance across the droplet, R_{l} as the thermal resistance across the lubricant and $R_{\mathrm{m/n/c/l}}$ as the thermal resistance imposed by the micro- and the nano-structures, the hydrophobic coating underneath the lubricant and the lubricant. In the absence of micro-structures, $R_{\mathrm{m/n/c/l}}$ is then replaced by $R_{\mathrm{n/c/l}}$ where only the presence of nano-structures, the coating and the lubricant between the structures is accounted for as for earlier reported superhydrophobic surfaces [9, 16, 83]. ΔT is the degree of subcooling typically defined as the temperature between the vapour and the condenser surface $\Delta T = T_{\mathrm{sat}} - T_{\mathrm{sub}}$. ΔT

is calculated taking into account the Kelvin effect ΔT_c due to droplet the curvature r, as: $\Delta T = T_v - T_s - \Delta T_c$ with $\Delta T_c = {}^{2T_{sat}\gamma_{wa}}/_{h_{fg} r \rho_w}$ [18, 84].

The interfacial thermal resistance is calculated as: $R_i = {}^{1}/_{h_i 2\pi r^2 (1-\cos\theta_a)}$ with h_i as the interfacial heat transfer coefficient $h_i = \frac{2\alpha}{(2-\alpha)} \frac{1}{\sqrt{2\pi R_g T_{sat}}} \frac{\rho_v h_{fg}^2}{T_{sat}}$, where α is the accommodation coefficient function of the condensation conditions and the amount of non-condensable gases [8, 9], R_g is the specific gas constant and ρ_v the water vapour specific density. All fluid and vapour properties were estimated at T_{sub}, whereas the accommodation coefficient is assumed as 0.04 as in the presence of condensable gases [2, 18]. The conduction thermal resistance across the droplet is estimated from the droplet size as: $R_d = {}^{\theta_a}/_{4\pi k_w r \sin\theta_a}$ where k_w is the water thermal resistance (k_w = 0.57 W/m/K). R_l is the heat transfer resistance imposed by the lubricant layer above the micro- and/or the nano-structures as: $R_l = {}^{\delta_l}/_{\pi r^2 k_l \sin^2\theta_a}$, where δ_o and k_o are the thickness and the thermal conductivity of the Kryotx® lubricant, respectively, which is neglected as per the impregnated emerged state reported. The heat transfer resistance imposed by the lubricant in between the micro- and the nano-structures will be then accounted for in $R_{m/n/c/l}$ and in $R_{n/c/l}$.

On one hand, in the absence of micro-structures, the thermal resistance between the base of the droplet and the solid surface $R_{n/c/l}$ can be considered as a resistance in parallel across the nano-structures and the coating, and across the coating and the lubricant present within the nano-structures. $R_{n/c/l}$ is then calculated as:

$$R_{n/c/l} = \frac{1}{\pi r^2 k_c \sin^2\theta_a} \left(\frac{k_{CuO} f_n}{\delta_c k_{CuO} + h_{CuO} k_c} + \frac{k_l (1-f_n)}{\delta_c k_l + h_{CuO} k_c} \right)^{-1} \quad \text{Eq. 3}$$

where k_c, k_{CuO} and k_l are the thermal conductivity of the hydrophobic coating (k_c = 0.2 W/m/K) [16], the copper oxide (k_{CuO} = 20 W/m/K) [2] and the Krytox® GPL103 (k_l = 0.09 W/m/K) [2], respectively. δ_c is the thickness of the hydrophobic coating (δ_c = 1 nm)[16] and h_{CuO} is the height of the nano-structures estimated from SEM and in agreement with Ref. 55 as h_{CuO} = 300 ± 20 nm [55]. While f_n is the solid fraction of nano-structures estimated from the Cassie-Baxter equation (solid fraction values from Table 1). Then, by substituting the different heat transfer resistances (i.e., the thermal resistance across the nano-structured SLIPS $R_{n/c/l}$, the droplet heat transfer resistance R_d and the condensation interfacial heat transfer resistance R_i) into Eq. 2, the theoretical heat transfer through a single condensing droplet and through the nano-structured SLIPS, i.e., in the absence of micro-structures, $q_{d/n/c/l}$ can be obtained as in Eq. 4:

$$q_{d/n/c/l} = \frac{\pi r^2 (T_v - T_s - \Delta T_c)}{\frac{1}{h_i 2(1-\cos\theta_a)} + \frac{r\theta_a}{4k_w \sin\theta_a} + \frac{1}{k_c \sin^2\theta_a}\left(\frac{k_{CuO} f_n}{\delta_c k_{CuO} + h_{CuO} k_c} + \frac{k_l(1-f_n)}{\delta_c k_l + h_{CuO} k_c}\right)^{-1}} \quad \text{Eq. 4}$$

On the other hand, in the presence of micro-structures the thermal resistance across the micro- and the nano-structures from the bulk surface to the condensing droplets must be considered as two paths in parallel as in Figure 6b. In the presence of micro-structures, for the area fraction corresponding to the solid fraction of micro-structures φ_m, the thermal resistance is exerted by the copper micro-structures and an additional resistance in parallel including the nano-structures and the coating and the lubricant and the coating as for the nano-structured case $R_{n/c/l}$, *i.e.*, Figure 6a and Eq. 3. The other path results from the area of void fraction (1-φ_m), i.e., absence of micro-structures, where a parallel resistance as in the nano-structured case including the nano-structures, the coating and the lubricant $R_{n/c/l}$ and the additional presence of lubricant in between the micro-structures must be accounted for. Then, $R_{m/n/c/l}$ is estimated as:

$$R_{m/n/c/l} = \varphi_m (R_{Cu} + R_{n/c/l}) + (1-\varphi_m)(R_l + R_{n/c/l}) \quad \text{Eq. 5}$$

where R_l is the resistance imposed by the lubricant impregnated between the micro-structures with thickness equivalent to the height of the micro-structures h_{Cu} (included as S_z in Table 1) as $R_l = h_{Cu}/\pi r^2 k_l \sin^2\theta_a$, while R_{Cu} is the resistance imposed by the micro-structures as $R_{Cu} = h_{Cu}/\pi r^2 k_{Cu} \sin^2\theta_a$. Then by substituting Eq. 3 and the different heat transfer resistances R_{Cu} and R_l into Eq. 5, the heat transfer resistance on a SLIPS in the presence of both micro- and nano-structures, the coating and the lubricant present in between the micro-and the nano-structures, $R_{m/n/c/l}$ can be rewritten as Eq. 6:

$$R_{m/n/c/l} = \varphi_m\left(\frac{h_{Cu}}{\pi r^2 k_{Cu}\sin^2\theta_a} + \frac{1}{\pi r^2 k_c \sin^2\theta_a}\left(\frac{k_{CuO} f_n}{\delta_c k_{CuO} + h_{CuO} k_c} + \frac{k_l(1-f_n)}{\delta_c k_l + h_{CuO} k_c}\right)^{-1}\right) + \\ + (1-\varphi_m)\left(\frac{h_l}{\pi r^2 k_l \sin^2\theta_a} + \frac{1}{\pi r^2 k_c \sin^2\theta_a}\left(\frac{k_{CuO} f_n}{\delta_c k_{CuO} + h_{CuO} k_c} + \frac{k_l(1-f_n)}{\delta_c k_l + h_{CuO} k_c}\right)^{-1}\right) \quad \text{Eq. 6}$$

Next, by substituting $R_{m/n/c/l}$ (Eq. 6) and the other heat transfer resistances, i.e., interfacial heat transfer resistance R_i and the heat transfer resistance through a condensing droplet R_d, into Eq. 2, the theoretical heat transfer across a single droplet and across the micro-/nano-structured SLIPS $q_{d/m/n/c/l}$ adopts the form of Eq. 7:

$$q_{d/m/n/c/l} = \frac{\pi r^2 (T_v - T_s - \Delta T_c)}{\frac{1}{h_i 2(1-\cos\theta_a)} + \frac{r\theta_a}{4k_w \sin\theta_a} + \left[\begin{array}{l} \varphi_m\left(\frac{h_{Cu}}{\pi r^2 k_{Cu}\sin^2\theta_a} + \frac{1}{\pi r^2 k_c \sin^2\theta_a}\left(\frac{k_{CuO} f_n}{\delta_c k_{CuO} + h_{CuO} k_c} + \frac{k_l(1-f_n)}{\delta_c k_l + h_{CuO} k_c}\right)^{-1}\right) + \\ + (1-\varphi_m)\left(\frac{h_l}{\pi r^2 k_l \sin^2\theta_a} + \frac{1}{\pi r^2 k_c \sin^2\theta_a}\left(\frac{k_{CuO} f_n}{\delta_c k_{CuO} + h_{CuO} k_c} + \frac{k_l(1-f_n)}{\delta_c k_l + h_{CuO} k_c}\right)^{-1}\right) \end{array}\right]} \quad \text{Eq. 7}$$

Next, Figure 7a includes the different heat transfer through individual condensing droplets including the nano-structured surface and the oil for n_{SLIPS} and N_{SLIPS} as $q_{d/n/c/l}$; and through individual condensing droplets, the micro-/nano-structures and the oil on Mn_{SLIPS} and mn_{SLIPS} surfaces as $q_{d/m/n/c/l}$, which are calculated by making use of Eq. 4 and Eq. 7, respectively. In addition, Figure 7b includes the droplet number density averaged for the different condensation times analysed (t = 5, 10, 15, 22 and 30 minutes) for Mn_{SLIPS}, mn_{SLIPS}, n_{SLIPS} and N_{SLIPS}:

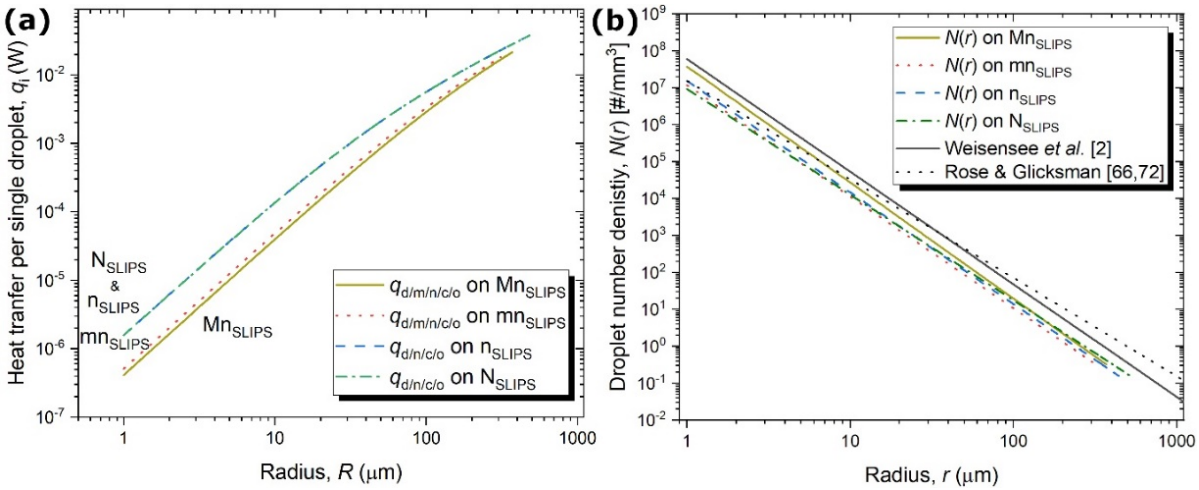

Figure 7 – (a) Theoretical heat transfer through single condensing droplets, q_i (W), versus droplet radius, r (μm), and (b) average droplet number density $N(r)$ [#/mm^3] versus droplet radius, r (μm), on Mn_{SLIPS} (gold solid line), mn_{SLIPS} (red dotted line), n_{SLIPS} (blue dashed line), and N_{SLIPS} (green dashed dotted line). Droplet number density power-law fitting proposed by Weisensee *et al.* is included in black solid line [2] and correlation developed by Rose and Glicksman is included in black dotted line [66, 72].

From Figure 7a, the different heat transfer through individual droplets function of the SLIPS underneath is presented. Clear differences when comparing the nano-structured n_{SLIPS} and N_{SLIPS} to the micro-/nano-structured Mn_{SLIPS} and mn_{SLIPS} are evident as a consequence of the greater heat transfer resistance imposed mainly by the lubricant present in between the micro-structures. Up to 50% greater heat transfer through individual droplets with sizes between 1 and few tens of micrometres (for droplets with sizes in the same order of magnitude or below to that of the micro-structures) is put forward on solely nano-structured n_{SLIPS} and N_{SLIPS} when compared to hierarchical ones Mn_{SLIPS} and mn_{SLIPS}. It is only when the size of the condensing droplets becomes one order of magnitude greater than that of the micro-structures when the heat transfer through single condensing droplets approaches that on nano-structured one as the thermal resistance through the condensing droplets becomes dominant when compared to the substrate thermal resistance. When comparing the two hierarchical micro-/nano-structured SLIPSs, lower heat transfer values are reported for Mn_{SLIPS} due to the greater size of the micro-

589 structures (see S_z in Table 1) and hence greater thickness of the lubricant in between the
590 structures hindering the heat transfer. When comparing the nano-structured SLIPS n_{SLIPS} and
591 N_{SLIPS} no appreciable quantitative differences are observed as the structural parameters were
592 similar, i.e., in the same orders of magnitude, despite of the different shape and geometry of
593 the nano-features. Similar discussion applies if considering the heat transfer through the solid
594 surface structure negligible when compared to the other thermal resistances.

595 The greater heat transfer through single droplets on n_{SLIPS} and N_{SLIPS} will presumably
596 provide better heat transfer performance given that there are no major appreciable shifts on the
597 droplet number density or on the droplet size distribution when compared to Mn_{SLIPS} and
598 mn_{SLIPS}. The droplet number density may vary as a consequence of the different interactions
599 between the condensate and the different structured SLIPSs shifting the trends towards smaller
600 or bigger sizes of the condensing droplets depending on their ability for droplet shedding [56].
601 When looking into the droplet number density reported in Figure 7b no major qualitative
602 differences are found when comparing the averaged trends for all SLIPSs studied. It is noted
603 though that up to 50% greater number of droplets for droplet sizes between 1 and 10 μm on
604 hierarchical Mn_{SLIPS} when compared to mn_{SLIPS}, n_{SLIPS} and N_{SLIPS}, presumably due to the better
605 droplet shedding performance of Mn_{SLIPS}. We stress here on the reasonable qualitative and
606 quantitative (within the same orders of magnitude) agreement on the droplet number
607 distribution when comparing this work to Weisensee *et al*., see Figure 7 [2].

608 Last, to obtain the theoretical surface heat flux q'', we couple the theoretical heat transfer
609 through individual condensing droplets in the presence ($q_{d/m/n/c/l}$) and absence of micro-
610 structures ($q_{d/n/c/l}$) reported in Figure 7a to the experimental droplet number density $N(r)$
611 reported in Figure 5 for droplets above the transition radius r_e at different intervals of time t on
612 the different SLIPSs studied. Figure 8 provides the average theoretical surface heat flux q''
613 calculated from the averaged droplet size distribution reported in Figure 5 and the theoretical

surface heat flux at specific condensation times making use of their *instantaneous* droplet size distribution at t = 5, 10, 15, 22 and 30 minutes also included in Figure 5. By representing the surface heat flux at different condensation times rather than the averaged one, the cyclic dynamic condensation heat transfer when making use of instantaneous droplet number densities for Mn_{SLIPS}, mn_{SLIPS}, n_{SLIPS}, and N_{SLIPS} is captured. Moreover, we would like to highlight here that the theoretical surface heat flux reported in Figure 8 might be overestimated as per the presumably lower concentration and temperature of the water vapour near the condensing surface when compared to the conditions assumed. Local depletion of the water vapour concentration near surfaces as per the experimental conditions adopted.

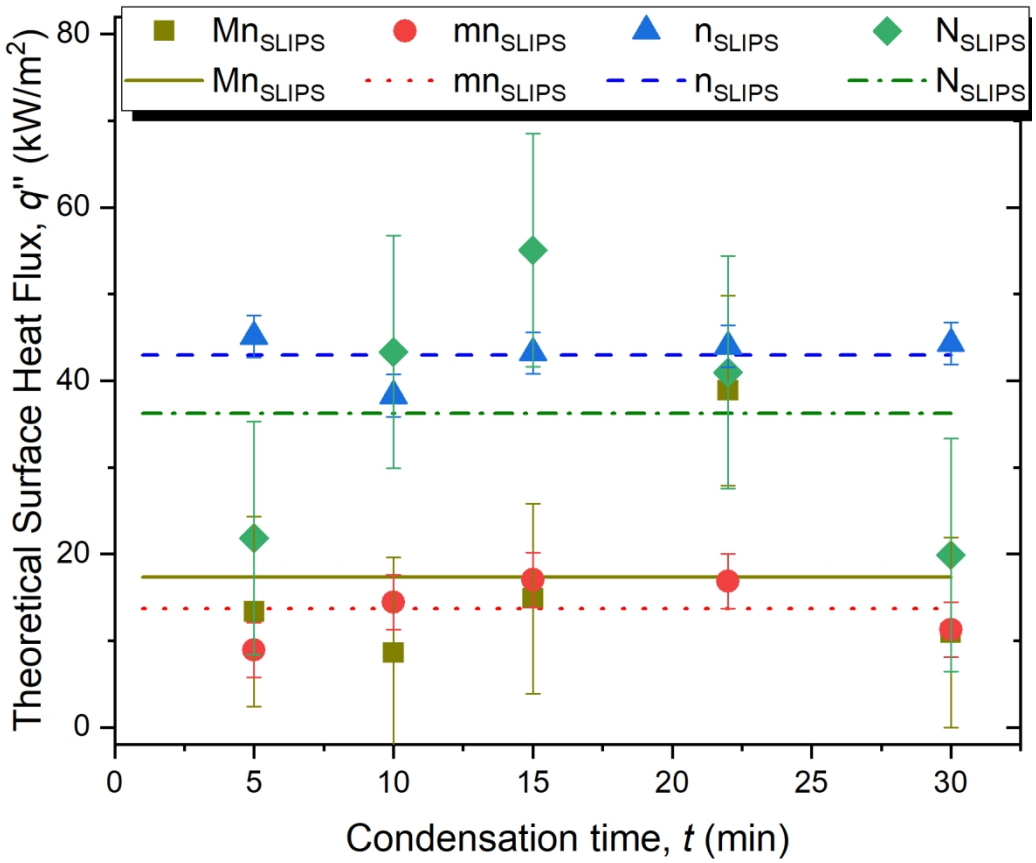

Figure 8 – Theoretical surface heat flux, q'' (kW/m²), versus time, t (minutes), on Mn_{SLIPS} (squares), mn_{SLIPS} (circles), n_{SLIPS} (up-triangles), and N_{SLIPS} (rhomboids), at t = 5, 10, 15, 22 and 30 minutes. Horizontal lines indicate the average theoretical surface heat flux, q'' (kW/m²), estimated from the average droplet number density reported in Figure 5 on Mn_{SLIPS} (solid line), mn_{SLIPS} (dotted line), n_{SLIPS} (dashed line) and N_{SLIPS} (dashed-dotted line). Error bars presented

have been calculated as the standard deviation of the different *instantaneous* theoretical heat surface heat flux for t = 5, 10, 15, 22 and 30 minutes for each SLIPSs.

From Figure 8, the high and homogeneous theoretical surface heat flux in the order of tens of kW/m^2 reported on the different SLIPSs is owed to the low adhesion of the droplets to the surface easing the continuous nucleation, growth and self-removal of the condensate in a continuous DWC manner[6, 22, 66]. When comparing the different SLIPSs, a 100% greater overall theoretical surface heat flux is reported in the absence of micro-structures, i.e., n_{SLIPS} and N_{SLIPS}, as a consequence of the reported 50% greater heat transfer through individual condensing droplets with sizes of tens of micrometres and smaller reported in Figure 7a. The presence of micro-structures exerts an additional heat transfer resistance through the micro-structures and the lubricant on Mn_{SLIPS} and mn_{SLIPS} when compared to nano-structured n_{SLIPS} and N_{SLIPS}, i.e., $R_{m/n/c/l} > R_{n/c/l}$; hence the lower theoretical surface heat flux reported on Mn_{SLIPS} and mn_{SLIPS}. Theoretical surface heat flux values reported here are found within 10 kW/m^2 to 60 kW/m^2, which are in the same range to those experimentally reported in the literature on SHSs[11, 68] and on SLIPS[47] between 10 kW/m^2 and 200 kW/m^2. The wide range of surface heat flux arises from the different thermal resistance of the substrate, type of fluid, presence or absence of non-condensable gases and/or subcooling conditions.

On a different note, the theoretical surface heat flux is also function of the droplet number density, which in turn shifts depending on the ability of the surface to shed the condensate. In the present case, the droplet size distribution for the hierarchical Mn_{SLIPS} is shifted towards greater number of small sized droplets while the droplet number density is also constrained to smaller droplet sizes as it was represented in Figure 5 and further summarized in Figure 7b. Despites the 50% greater droplet number density found for droplet sizes between 1 μm and 10 μm on hierarchical Mn_{SLIPS} (Figure 7b), the additional heat transfer resistance imposed by the micro-structures and the lubricant limits the heat transfer through individual droplets $q_{d/m/n/c/l}$

654 when compared to nano-structured n_{SLIPS} and N_{SLIPS}, i.e., $q_{d/m/n/c/l} < q_{d/n/c/l}$. As a consequence,
655 the heat transfer performance on hierarchical SLIPSs is lower than that of nano-structured ones.
656 Last, we would like to highlight the cyclic oscillatory nature of the heat transfer values reported
657 in Figure 8 for each of the SLIPSs studied. Theoretical heat transfer values in Figure 8 are
658 sensitive to the droplet number density $N(r)$ as per the different droplet number density versus
659 time reported in Figure 5 and Table 2.

660

Conclusions

An experimental investigation on the condensation performance of hierarchical micro- and nano- and on nano-structured slippery lubricant infused porous surfaces (SLIPSs) has been carried out. Two hierarchical micro-/nano-structured SLIPSs varying in the size and density of the micro-structures and two nano-structured ones have been fabricated and observed under optical microscopy and at the macroscale during condensation phase-change. From experimental observations the average droplet number density and the droplet number density at different condensation times (t = 1, 5, 10, 15, 22 and 30 minutes) have been extracted and plotted versus droplet size. Different droplet number density and different maximum droplet radius are reported depending on the SLIPSs and the condensation times studied. Up to 50% greater droplet number density is reported on the hierarchical Mn_{SLIPS} for droplets sizes between 1 and 10 micrometres, which is owed to the ability of this hierarchical surface to shed the condensate shifting the droplet number density towards smaller sizes allowing for a greater number of condensing droplets. Moreover, the transient nature of the droplet number density is pointed out as one of the additional contribution of this work. Furthermore, resistance based model earlier proposed for nano-structured superhydrophobic and lubricant infused surfaces is revisited to account for the heat transfer through individual droplets in the presence of micro-structures and nano-structures and the lubricant. A 50% greater heat transfer is achieved through individual droplets in the absence of micro-structures when compared to hierarchical SLIPSs caused by the absence of the additional thermal resistance imposed by the micro-structures and the lubricant. Then, by coupling the heat transfer through individual droplets to the droplet number density, the overall surface heat flux and the heat flux at different condensation times is estimated. Up to 100% greater overall heat transfer performance is estimated on nano-structured SLIPS (n_{SLIPS} and N_{SLIPS}) when compared to hierarchical ones (Mn_{SLIPS} and mn_{SLIPS}). Findings presented here are of importance for the optimisation and characterisation of SLIPS for condensation heat transfer and other related applications.

Acknowledgments

D.O and Y.T. acknowledge the support received from the International Institute for Carbon-Neutral Energy Research (WPI-I^{2}CNER) and the Ministry of Education, Culture, Sports, Science and Technology, Japan (MEXT). D.O. greatly acknowledges the support received by the Japanese Society for the Promotion of Science (JSPS) KAKENHI, Japan (Grant No. JP18K13703 and). P.Z. and F.Y.L. acknowledge the support of the National Natural Science Foundation of China (Contract No. 51976117). F.Y.L. acknowledges the Natural Science Foundation of Shanghai, China (Contract No. 19ZR1401700). The authors acknowledge Dr. Sumitomo Hidaka from Kyushu University for his help and assistance on the experimental setup. The authors acknowledge Professor Aleksandr N. Pavlenko (chair) and Dr. Anton Surtaev (scientific secretary), organisers of the 5th International Workshop on Heat-Mass Transfer Advances for Energy Conservation and Pollution Control held in Novosibirsk Russia, for the hospitality, successful organisation and the invitation to submit this work as special issue in Applied Thermal Engineering.

Notes

The authors declare no competing financial interests.

Graphical Abstract

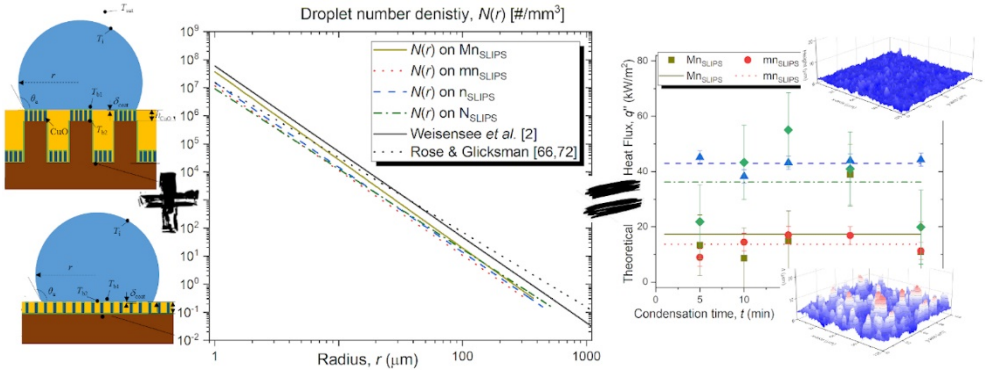

References

[1] J.M. Beér, High efficiency electric power generation: The environmental role, Progress in Energy and Combustion Science, 33 (2007) 107-134.

[2] P.B. Weisensee, Y. Wang, Q. Hongliang, D. Schultz, W.P. King, N. Miljkovic, Condensate droplet size distribution on lubricant-infused surfaces, International Journal of Heat and Mass Transfer, 109 (2017) 187-199.

[3] E.J. Le Fevre, J.W. Rose, An experimental study of heat transfer by dropwise condensation, International Journal of Heat and Mass Transfer, 8 (1965) 1117-1133.

[4] H.-Y. Kim, H.J. Lee, B.H. Kang, Sliding of Liquid Drops Down an Inclined Solid Surface, Journal of Colloid and Interface Science, 247 (2002) 372-380.

[5] S. Vemuri, K.J. Kim, An experimental and theoretical study on the concept of dropwise condensation, International Journal of Heat and Mass Transfer, 49 (2006) 649-657.

[6] D. Attinger, C. Frankiewicz, A.R. Betz, T.M. Schutzius, R. Ganguly, A. Das, C.-J. Kim, C.M. Megaridis, Surface engineering for phase change heat transfer: A review, MRS Energy & Sustainability, 1 (2014).

[7] A. Umur, P. Griffith, Mechanism of Dropwise Condensation, Journal of Heat Transfer, 87 (1965) 275-282.

[8] C. Graham, P. Griffith, Drop size distributions and heat transfer in dropwise condensation, International Journal of Heat and Mass Transfer, 16 (1973) 337-346.

[9] N. Miljkovic, R. Enright, E.N. Wang, Effect of Droplet Morphology on Growth Dynamics and Heat Transfer during Condensation on Superhydrophobic Nanostructured Surfaces, ACS Nano, 6 (2012) 1776-1785.

[10] C.-H. Chen, Q. Cai, C. Tsai, C.-L. Chen, G. Xiong, Y. Yu, Z. Ren, Dropwise condensation on superhydrophobic surfaces with two-tier roughness, Applied Physics Letters, 90 (2007) 173108.

[11] N. Miljkovic, R. Enright, Y. Nam, K. Lopez, N. Dou, J. Sack, E.N. Wang, Jumping-Droplet-Enhanced Condensation on Scalable Superhydrophobic Nanostructured Surfaces, Nano Letters, 13 (2013) 179-187.

[12] R. Parin, A. Martucci, M. Sturaro, S. Bortolin, M. Bersani, F. Carraro, D. Del Col, Nano-structured aluminum surfaces for dropwise condensation, Surface and Coatings Technology, 348 (2018) 1-12.

[13] M.D. Mulroe, B.R. Srijanto, S.F. Ahmadi, C.P. Collier, J.B. Boreyko, Tuning Superhydrophobic Nanostructures To Enhance Jumping-Droplet Condensation, ACS Nano, 11 (2017) 8499-8510.

[14] E. Ölçeroğlu, M. McCarthy, Self-Organization of Microscale Condensate for Delayed Flooding of Nanostructured Superhydrophobic Surfaces, ACS Applied Materials & Interfaces, 8 (2016) 5729-5736.

[15] J.B. Boreyko, C.-H. Chen, Self-Propelled Dropwise Condensate on Superhydrophobic Surfaces, Physical Review Letters, 103 (2009) 184501.

[16] R. Enright, N. Miljkovic, N. Dou, Y. Nam, E.N. Wang, Condensation on Superhydrophobic Copper Oxide Nanostructures, Journal of Heat Transfer, 135 (2013) 091304-091304-091312.

[17] R. Parin, M. Sturaro, S. Bortolin, A. Martucci, D. Del Col, Heat transfer during dropwise condensation of steam over a mirror polished sol-gel coated aluminum substrate, International Journal of Thermal Sciences, 144 (2019) 93-106.

[18] S. Chavan, H. Cha, D. Orejon, K. Nawaz, N. Singla, Y.F. Yeung, D. Park, D.H. Kang, Y. Chang, Y. Takata, N. Miljkovic, Heat Transfer through a Condensate Droplet on Hydrophobic and Nanostructured Superhydrophobic Surfaces, Langmuir, 32 (2016) 7774-7787.

[19] S. Kim, K.J. Kim, Dropwise Condensation Modeling Suitable for Superhydrophobic Surfaces, Journal of Heat Transfer, 133 (2011) 081502-081502-081508.

[20] A. Lafuma, D. Quéré, Superhydrophobic states, Nature Materials, 2 (2003) 457.

[21] C. Neinhuis, W. Barthlott, Characterization and Distribution of Water-repellent, Self-cleaning Plant Surfaces, Annals of Botany, 79 (1997) 667-677.

[22] D. Orejon, O. Shardt, N.S.K. Gunda, T. Ikuta, K. Takahashi, Y. Takata, S.K. Mitra, Simultaneous dropwise and filmwise condensation on hydrophilic microstructured surfaces, International Journal of Heat and Mass Transfer, 114 (2017) 187-197.
[23] D. Orejon, O. Shardt, P.R. Waghmare, N.S. Kumar Gunda, Y. Takata, S.K. Mitra, Droplet migration during condensation on chemically patterned micropillars, RSC Advances, 6 (2016) 36698-36704.
[24] P.S. Mahapatra, A. Ghosh, R. Ganguly, C.M. Megaridis, Key design and operating parameters for enhancing dropwise condensation through wettability patterning, International Journal of Heat and Mass Transfer, 92 (2016) 877-883.
[25] E. Ölçeroğlu, C.-Y. Hsieh, K.K.S. Lau, M. McCarthy, Thin Film Condensation Supported on Ambiphilic Microstructures, Journal of Heat Transfer, 139 (2017) 020910-020910-020911.
[26] R.L. Winter, M. McCarthy, Dewetting from Amphiphilic Minichannel Surfaces during Condensation, ACS Applied Materials & Interfaces, (2020).
[27] J. Oh, R. Zhang, P.P. Shetty, J.A. Krogstad, P.V. Braun, N. Miljkovic, Thin Film Condensation on Nanostructured Surfaces, Advanced Functional Materials, 1707000-n/a.
[28] Y. Shang, Y. Hou, M. Yu, S. Yao, Modeling and optimization of condensation heat transfer at biphilic interface, International Journal of Heat and Mass Transfer, 122 (2018) 117-127.
[29] Y. Hou, M. Yu, X. Chen, Z. Wang, S. Yao, Recurrent Filmwise and Dropwise Condensation on a Beetle Mimetic Surface, ACS Nano, 9 (2015) 71-81.
[30] D. Orejon, A. Askounis, Y. Takata, D. Attinger, Dropwise Condensation on Multiscale Bioinspired Metallic Surfaces with Nanofeatures, ACS Applied Materials & Interfaces, 11 (2019) 24735-24750.
[31] X. Yan, Z. Huang, S. Sett, J. Oh, H. Cha, L. Li, L. Feng, Y. Wu, C. Zhao, D. Orejon, F. Chen, N. Miljkovic, Atmosphere-Mediated Superhydrophobicity of Rationally Designed Micro/Nanostructured Surfaces, ACS Nano, 13 (2019) 4160-4173.
[32] D.J. Preston, N. Miljkovic, J. Sack, R. Enright, J. Queeney, E.N. Wang, Effect of hydrocarbon adsorption on the wettability of rare earth oxide ceramics, Applied Physics Letters, 105 (2014) 011601.
[33] L.B. Boinovich, A.M. Emelyanenko, A.S. Pashinin, C.H. Lee, J. Drelich, Y.K. Yap, Origins of Thermodynamically Stable Superhydrophobicity of Boron Nitride Nanotubes Coatings, Langmuir, 28 (2012) 1206-1216.
[34] H.F. Bohn, W. Federle, Insect aquaplaning: *Nepenthes* pitcher plants capture prey with the peristome, a fully wettable water-lubricated anisotropic surface, Proceedings of the National Academy of Sciences of the United States of America, 101 (2004) 14138-14143.
[35] T.-S. Wong, S.H. Kang, S.K.Y. Tang, E.J. Smythe, B.D. Hatton, A. Grinthal, J. Aizenberg, Bioinspired self-repairing slippery surfaces with pressure-stable omniphobicity, Nature, 477 (2011) 443-447.
[36] T.-S. Wong, T. Sun, L. Feng, J. Aizenberg, Interfacial materials with special wettability, MRS Bulletin, 38 (2013) 366-371.
[37] J.D. Smith, R. Dhiman, S. Anand, E. Reza-Garduno, R.E. Cohen, G.H. McKinley, K.K. Varanasi, Droplet mobility on lubricant-impregnated surfaces, Soft Matter, 9 (2013) 1772-1780.
[38] C. Hao, J. Li, Y. Liu, X. Zhou, Y. Liu, R. Liu, L. Che, W. Zhou, D. Sun, L. Li, L. Xu, Z. Wang, Superhydrophobic-like tunable droplet bouncing on slippery liquid interfaces, Nature Communications, 6 (2015) 7986.
[39] K. Rykaczewski, A.T. Paxson, M. Staymates, M.L. Walker, X. Sun, S. Anand, S. Srinivasan, G.H. McKinley, J. Chinn, J.H.J. Scott, K.K. Varanasi, Dropwise Condensation of Low Surface Tension Fluids on Omniphobic Surfaces, Scientific Reports, 4 (2014) 4158.
[40] J.B. Boreyko, G. Polizos, P.G. Datskos, S.A. Sarles, C.P. Collier, Air-stable droplet interface bilayers on oil-infused surfaces, Proceedings of the National Academy of Sciences, 111 (2014) 7588-7593.
[41] S. Nishimoto, B. Bhushan, Bioinspired self-cleaning surfaces with superhydrophobicity, superoleophobicity, and superhydrophilicity, RSC Advances, 3 (2013) 671-690.
[42] B.R. Solomon, K.S. Khalil, K.K. Varanasi, Drag Reduction using Lubricant-Impregnated Surfaces in Viscous Laminar Flow, Langmuir, 30 (2014) 10970-10976.

[43] P. Kim, T.-S. Wong, J. Alvarenga, M.J. Kreder, W.E. Adorno-Martinez, J. Aizenberg, Liquid-Infused Nanostructured Surfaces with Extreme Anti-Ice and Anti-Frost Performance, ACS Nano, 6 (2012) 6569-6577.
[44] K.-C. Park, P. Kim, A. Grinthal, N. He, D. Fox, J.C. Weaver, J. Aizenberg, Condensation on slippery asymmetric bumps, Nature, advance online publication (2016).
[45] R. Xiao, N. Miljkovic, R. Enright, E.N. Wang, Immersion Condensation on Oil-Infused Heterogeneous Surfaces for Enhanced Heat Transfer, Scientific Reports, 3 (2013) 1988.
[46] D.J. Preston, Z. Lu, Y. Song, Y. Zhao, K.L. Wilke, D.S. Antao, M. Louis, E.N. Wang, Heat Transfer Enhancement During Water and Hydrocarbon Condensation on Lubricant Infused Surfaces, Scientific Reports, 8 (2018) 540.
[47] S. Sett, P. Sokalski, K. Boyina, L. Li, K.F. Rabbi, H. Auby, T. Foulkes, A. Mahvi, G. Barac, L.W. Bolton, N. Miljkovic, Stable Dropwise Condensation of Ethanol and Hexane on Rationally Designed Ultrascalable Nanostructured Lubricant-Infused Surfaces, Nano Letters, 19 (2019) 5287-5296.
[48] X. Dai, B.B. Stogin, S. Yang, T.-S. Wong, Slippery Wenzel State, ACS Nano, 9 (2015) 9260-9267.
[49] S. Yang, R. Qiu, H. Song, P. Wang, Z. Shi, Y. Wang, Slippery liquid-infused porous surface based on perfluorinated lubricant/iron tetradecanoate: Preparation and corrosion protection application, Applied Surface Science, 328 (2015) 491-500.
[50] S.B. Subramanyam, G. Azimi, K.K. Varanasi, Designing Lubricant-Impregnated Textured Surfaces to Resist Scale Formation, Advanced Materials Interfaces, 1 (2014) 1300068.
[51] S. Anand, A.T. Paxson, R. Dhiman, J.D. Smith, K.K. Varanasi, Enhanced Condensation on Lubricant-Impregnated Nanotextured Surfaces, ACS Nano, 6 (2012) 10122-10129.
[52] D. Daniel, M.N. Mankin, R.A. Belisle, T.-S. Wong, J. Aizenberg, Lubricant-infused micro/nano-structured surfaces with tunable dynamic omniphobicity at high temperatures, Applied Physics Letters, 102 (2013) 231603.
[53] K.-C. Park, P. Kim, A. Grinthal, N. He, D. Fox, J.C. Weaver, J. Aizenberg, Condensation on slippery asymmetric bumps, Nature, 531 (2016) 78.
[54] X. Zhu, Z. Zhang, X. Men, J. Yang, X. Xu, Rapid Formation of Superhydrophobic Surfaces with Fast Response Wettability Transition, ACS Applied Materials & Interfaces, 2 (2010) 3636-3641.
[55] P. Zhang, Y. Maeda, F. Lv, Y. Takata, D. Orejon, Enhanced Coalescence-Induced Droplet-Jumping on Nanostructured Superhydrophobic Surfaces in the Absence of Microstructures, ACS Applied Materials & Interfaces, 9 (2017) 35391-35403.
[56] D. Orejon, Y. Maeda, F. Lv, P. Zhang, Y. Takata, Effect of Microstructures on Superhydrophobic and Slippery Lubricant-Infused Porous Surfaces During Condensation Phase-Change, in: ASME 2018 16th International Conference on Nanochannels, Microchannels, and Minichannels, 2018.
[57] P. Zhang, F.Y. Lv, A. Askounis, D. Orejon, B. Shen, Role of impregnated lubricant in enhancing thermosyphon performance, International Journal of Heat and Mass Transfer, 109 (2017) 1229-1238.
[58] S. Zarei, H.R. Talesh Bahrami, H. Saffari, Effects of geometry and dimension of micro/nano-structures on the heat transfer in dropwise condensation: A theoretical study, Applied Thermal Engineering, 137 (2018) 440-450.
[59] L. Liu, F. Xu, L. Ma, Facile Fabrication of a Superhydrophobic Cu Surface via a Selective Etching of High-Energy Facets, The Journal of Physical Chemistry C, 116 (2012) 18722-18727.
[60] F.Y. Lv, P. Zhang, Fabrication and characterization of superhydrophobic surfaces on aluminum alloy substrates, Applied Surface Science, 321 (2014) 166-172.
[61] K. Matsumoto, H. Inaba, K. Murahashi, K. Hayashi, D. Shirai, M. Honda, T. Ikeya, K. Matsunaga, Investigation on controlling ice adhesion force to solid surface by using thin film made from silane-coupler, International Journal of Refrigeration, 36 (2013) 862-869.
[62] D. Quéré, Wetting and Roughness, Annual Review of Materials Research, 38 (2008) 71-99.
[63] ImageJ, ImageJ 1.50b Wayne Rasband, National Institutes of Health, USA, last checked: April 2016, URL http://imagej.nih.gov/ij, in.

[64] A.F. Stalder, G. Kulik, D. Sage, L. Barbieri, P. Hoffmann, A snake-based approach to accurate determination of both contact points and contact angles, Colloids and Surfaces A: Physicochemical and Engineering Aspects, 286 (2006) 92-103.
[65] S. Sett, X. Yan, G. Barac, L.W. Bolton, N. Miljkovic, Lubricant-Infused Surfaces for Low-Surface-Tension Fluids: Promise versus Reality, ACS Applied Materials & Interfaces, 9 (2017) 36400-36408.
[66] J.W. Rose, L.R. Glicksman, Dropwise condensation—The distribution of drop sizes, International Journal of Heat and Mass Transfer, 16 (1973) 411-425.
[67] Image-Pro Plus 6.0, Media Cybermetics, Inc., USA, http://www.mediacy.com/imageproplus, in.
[68] R. Wen, Q. Li, J. Wu, G. Wu, W. Wang, Y. Chen, X. Ma, D. Zhao, R. Yang, Hydrophobic copper nanowires for enhancing condensation heat transfer, Nano Energy, 33 (2017) 177-183.
[69] J.R. Maa, Drop size distribution and heat flux of dropwise condensation, The Chemical Engineering Journal, 16 (1978) 171-176.
[70] X. Liu, P. Cheng, Dropwise condensation theory revisited: Part I. Droplet nucleation radius, International Journal of Heat and Mass Transfer, 83 (2015) 833-841.
[71] R. Wen, Z. Lan, B. Peng, W. Xu, X. Ma, Droplet dynamics and heat transfer for dropwise condensation at lower and ultra-lower pressure, Applied Thermal Engineering, 88 (2015) 265-273.
[72] J.W. Rose, Further aspects of dropwise condensation theory, International Journal of Heat and Mass Transfer, 19 (1976) 1363-1370.
[73] H. Tanaka, Measurements of Drop-Size Distributions During Transient Dropwise Condensation, Journal of Heat Transfer, 97 (1975) 341-346.
[74] I. Tanasawa, Advances in Condensation Heat Transfer, in: J.P. Hartnett, T.F. Irvine, Y.I. Cho (eds.) Advances in Heat Transfer, Vol. 21, Elsevier, 1991, pp. 55-139.
[75] N. Watanabe, M. Aritomi, A. Machida, Time-series characteristics and geometric structures of drop-size distribution density in dropwise condensation, International Journal of Heat and Mass Transfer, 76 (2014) 467-483.
[76] C. Yamali, H. Merte Jr, A theory of dropwise condensation at large subcooling including the effect of the sweeping, Heat and Mass Transfer, 38 (2002) 191-202.
[77] J.W. Rose, Dropwise condensation theory, International Journal of Heat and Mass Transfer, 24 (1981) 191-194.
[78] J. Sun, P.B. Weisensee, Microdroplet self-propulsion during dropwise condensation on lubricant-infused surfaces, Soft Matter, 15 (2019) 4808-4817.
[79] X. Liu, P. Cheng, Dropwise condensation theory revisited Part II. Droplet nucleation density and condensation heat flux, International Journal of Heat and Mass Transfer, 83 (2015) 842-849.
[80] V.P. Carey, Liquid Vapor Phase Change Phenomena: An Introduction to the Thermophysics of Vaporization and Condensation Processes in Heat Transfer Equipment, Second Edition, Taylor & Francis, 2007.
[81] N. Miljkovic, R. Enright, E.N. Wang, Modeling and Optimization of Superhydrophobic Condensation, Journal of Heat Transfer, 135 (2013).
[82] E. Alizadeh-Birjandi, A. Alshehri, H.P. Kavehpour, Condensation on Surfaces With Biphilic Topography: Experiment and Modeling, Frontiers in Mechanical Engineering, 5 (2019).
[83] N. Miljkovic, E.N. Wang, Condensation heat transfer on superhydrophobic surfaces, MRS Bulletin, 38 (2013) 397-406.
[84] L. Zheng, Y.-X. Wang, J.L. Plawsky, P.C. Wayner, Effect of Curvature, Contact Angle, and Interfacial Subcooling on Contact Line Spreading in a Microdrop in Dropwise Condensation, Langmuir, 18 (2002) 5170-5177.